Data-driven modeling of thermal history in additive manufacturing

Mriganka Roy*[1] and Olga Wodo†[2]

[1]Department of Mechanical and Aerospace Engineering
[2]Department of Material Design and Innovation

May 20, 2019

Abstract

Additive manufacturing (AM) has the potential to construct complex geometries through the simple and highly repetitive process of layer-by-layer deposition. The process is repetitive and fully automated, but the interactions between layers during deposition are tightly coupled. To unravel these interactions the computational models of the manufacturing process are critically needed. However, current state-of-the-art physics-based models are computationally demanding and cannot be used for any realistic optimization. To address this challenge we build a surrogate model (SM) of thermal profiles that significantly reduces the computational cost. We build this model based on the observation that any AM process exhibits a high level of redundancy and periodicity, making it an ideal problem for machine learning and surrogate modeling.

We introduce a unique geometry representation that is the key insight for this work. Rather than directly using the part geometry, we parameterize the gcode for a given geometry into a set of local distances from heat sources (laser, extruder) and sinks (cooling surfaces). This set of distances is directly used as an input for the SM of thermal history. Since this set can be calculated a priori from gcode, the explicit geometry considerations are largely factored out. Moreover, we leverage the analytical solution to the moving heat source model to determine heat influence zone (HIZ). The size of HIZ allows deciding a priori what should be the cardinality of the distance sets. We show that for fused filament fabrication the size of HIZ is small; thus, the number of input variables for the SM is small as well.

To build the SM, we first generate the thermal data using physics-based model and use it to train an artificial neural network model. We train the SM and demonstrate its high predictive power and low computational cost. Specifically, we demonstrate the capabilities of our model to construct the thermal history for any point with acceptable accuracy (error below 5.0%) in almost real time (0.034 s for any point in the part). With such performance, this model opens the possibility of optimization as well as process planning, and in-situ monitoring for closed-loop control.

*mriganka@buffalo.edu
†olgawodo@buffalo.edu

1 Introduction

Additive manufacturing (AM) is an emerging technology that enables fabrication of 3D objects by depositing layers of material, one after another. At this stage, a wide range of material classes can be printed, such as plastic [4], metals [10, 33], food [28, 27], ceramics [11, 55, 60], and bio-materials [30]. Initially, AM was conceptualized as a tool for rapid prototyping and visualization, due to its ease of building very complex geometries. The increased popularity of AM lead to increased interest in the process dynamics, but its understanding is still mostly lacking, which is hampering the rational design of the process and part properties.

A significant progress has been made to understand the process dynamics both on the modeling [2, 25, 45] and experimental front [1, 40, 52]. For example, relations between the process parameters, thermal profile and the strength of the printed parts were established empirically [40]. Experiments were also conducted to find the degree of consolidation of the deposited filaments [52]. The effects of the printing parameters (such as deposition speed, road size, deposition pattern, deposition temperature, and environment temperature) on the mesostructure of the printed parts were studied in details [58, 59, 53]. Although very insightful, the experimental investigations are expensive and quite often have limited scope. For example, once the layer is buried under the next layer, the physical access to measure the temperature is mostly limited. This limitation is not present in case of modeling, where high spatial and temporal resolution is theoretically possible. Mathematical models can range from examining the behavior of the polymers during the bonding process of the deposited filaments at the micrometer scale [4] to estimating the deformation in the printed part at centimeter scale [59]. Computational model can also be used to estimate the degree of consolidation in printed polymers [46]. However, the main challenges with computational models are strongly tied to the high computational cost, large memory requirements, and long computing time required to predict the deposition process. Interestingly, in the current state, it is faster to print and test the part for properties than to analyze the deposition process through simulations.

To address the computational challenge numerous approaches have been explored including analytical models [49, 50], adaptive meshing [38], and domain decomposition [5]. Patil *et al.* [41] created an efficient finite element based model utilizing multi-scale simulation with adaptive mesh refinement and de-refinement to reduce computational cost without affecting the accuracy of the results. Nevertheless, these methods still require high computational resources that are beyond any optimization of a large part. In [49], Steuben *et al.* formulated an analytical model capable of analyzing the thermal behavior of a metal printing process at a lower computational cost. The analytical solutions were used to ensemble time history using "method of images" that were additionally enriched by several functions to capture the high non-linearity in the geometries and material properties. A large reduction in computational time was reported for a selected geometry. However, that approach still requires specific enrichment functions for many factors (e.g., the latent heat from melting and resolidification). Moreover, compensation functions must be tuned for specific geometries.

Another model that reported a high reduction in computational time is work by Stockman *et al.* [50]. A three dimensional finite difference based thermal model has been developed for AM processes to reduce the computation time by leveraging coarse meshing in both time and space along with simplifying

assumptions about the underlying processes. The model was tested on a print size with 31 layers, each layer being 127 mm long with 80 roads. The computation time was 22 minutes which is still high. Neiva *et al.* [34] implemented a finite element framework that was parallelized by domain decomposition and adaptive meshing and led to reduction in the computational cost. All these models surpass traditional modeling in speed while maintaining a certain degree of accuracy, but do not enable in-situ control or process optimization.

In this paper, we present another approach that aims at replacing the computational model of layer-by-layer deposition with its statistical surrogate, also known as a Surrogate Model (SM) [42, 36]. As the name suggests, the surrogate model works as the computationally inexpensive alternative of a relatively more expensive physics based model. SM is commonly used in aerospace engineering [26, 19] and biological sciences [17]. In the area of AM, SM has been explored only with limited capacity and scope. For example, a Gaussian process-based surrogate model has been built for Laser Power-Bed fusion process [54]. The SM maps process parameters (laser power, beam size, and scan speed) to the selected feature of the deposition (i.e., depth of the melt pool). The model was trained from limited experimental data and predicted the melt pool depth with acceptable accuracy. Another surrogate model has been built for a bottom-up stereolithography process to map pull-up separation stress to shape of layers [56]. Specifically, the model predicts the separation stress for different geometries without performing a costly finite element simulations. The model allows choosing the process parameter that ensures the processing of the part rather than predicting the coupled effect of the layer by layer deposition.

The work of Mozaffar *et al.* [32] is the most relevant work for this paper, as it focuses on predicting temperature profiles for various geometries. Mozaffar *et al.* proposed a data driven approach to predict the thermal history in a direct energy deposition process using recurrent neural networks. The model mapped the position of a point on the printing surface, time of deposition, distance of the closest cooling surface, and laser parameters with the thermal output (i.e., temperature profile). Authors reported high accuracy of the predicted thermal profiles for a longer period of printing than the training and dissimilar geometry. Although the model shows high competency, it required a large data set (250,000 points) to train the model. Generating such large quantities of data is time-consuming. The model is also based on two hand picked geometrical features (distance from nearest boundary and layer height), which may limits its generalizability to other more complex geometries.

Finally, Francis J. [13] predicted distortion of a laser-based AM process through deep learning. Similar to the previous model, a large number of images (21,818, size: 40GB) captured from the experiments were used to train the convolutional and artificial neural network. Moreover, that model mostly focused on mapping process variables to part properties while omitting the specific interactions occurring during the deposition process, including the effect of the geometry. Consequently, these models have limited capabilities to perform a rational design of the deposition process or closed-loop control.

In this paper, we address this gap by devising the SM capable of predicting the deposition history for the entire part geometries. Rather than focusing on one quantity of interest, e.g., melt pool depth, we aim at predicting the entire thermal profile for any point in the part. In particular, we build our SM by leveraging the high level of redundancy, repeatability, and periodicity that exists in AM processes. We hypothesize that if the pattern exists in the deposition behavior, it can be captured using machine learning, and subsequently used to predict the behavior of another part. We build the model in two

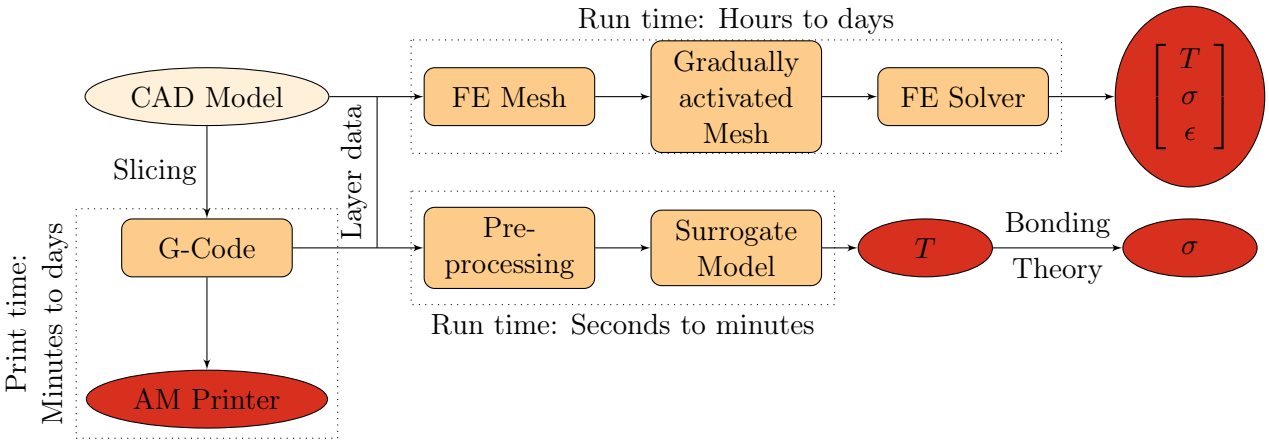

Figure 1: Overview of steps involved in any AM process, and link with physics-based prediction and data-driven approach (presented in this paper).

steps. First use the physics-based numerical model to generate the data required to train the surrogate model. In the second step, we leverage the neural network to build SM of thermal behavior. We showcase the model by predicting the thermal behavior of Fused Filament Fabrication (FFF) process. We used 26,000 data points (5.5 MB) for training the surrogate model. Our model is capable of predicting the thermal behavior with high accuracy (error below 5%) with almost real-time response (0.036 s per point) for extrapolative and interpolative cases. Our SM opens the avenue for *in-situ* process control, process optimization and materials design for processing process.

2 Unique characteristics of additive manufacturing

Additive Manufacturing processes have two unique characteristics: additive and repetitive character. Any AM process follows a generic procedure to build a part, as depicted in Figure 1. First, the CAD model of the 3D part is designed. Next, the CAD model is partitioned into roads and layers by a slicing software. In this process, the CAD model is translated into the set of simple and repetitive instructions encoded in the gcode file that has been generated for a specific part. As a consequence of this step, through the slicing process, the geometry of the part is effectively factored out.

On the modeling front, the traditional discrete models (e.g., FEM) follow a very similar workflow. The CAD model is discretized into the computational mesh. During the simulations, the mesh is gradually activated mimicking gcode instructions along with the corresponding system of equations being assembled and solved. The inevitable consequence of such setup is the additive computational cost that increases as the deposition proceeds. The total run-time depends on the size of the part, but in general, it ranges from hours to even days. For example, Zhang et al. [59] conducted the thermodynamic simulations for a specimen of size $40 \times 10 \times 1.016\ mm$ composed of 1600 discrete depositions. In total, authors reported that the simulation required $30 \sim 35$ hours using a 2.8 GHz processor with $2GB$ memory.

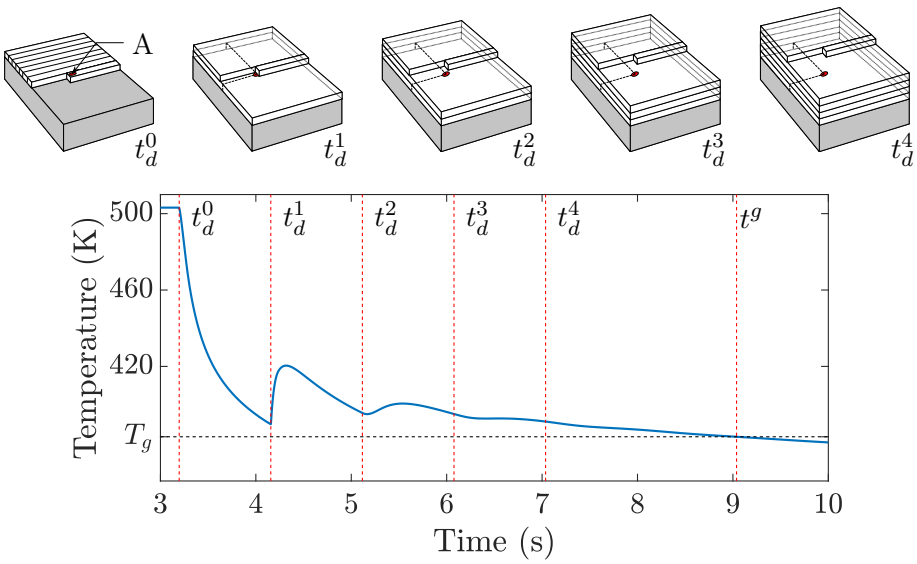

Figure 2: Cyclic reheating in the temperature profile at an interior point (A). At time t_d^0 the point is deposited and at t_d^i the i^{th} reheating cycle begins due to an influencing deposition as shown in the schematic diagrams above them.

The additive nature of the traditional physics-based models mimics well the additive nature of the deposition process. However, the ensemble of the part geometry still remains the integral element of these models. With such a problem setup, it is challenging to exploit the repetitive nature of the deposition process. Consequently, most of the calculations in traditional methodology may become redundant. In this work, we formulate the SM that does not rely explicitly on the geometry of the entire part. Below we include the critical features that guided the formulation of our SM:

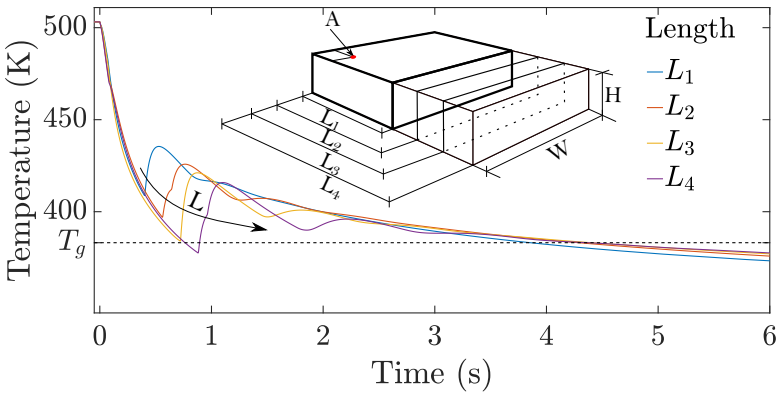

Figure 3: Pattern in the temperature profile with respect to print size at an interior point A (Position: top of 1st layer and 1st road).

- **Cyclic reheating:** Cyclic reheating is a signature of the road-wise and layer-wise heat influx

from the depositions. The cyclic reheating in the temperature profile is typical for any thermally driven AM process and is observed for any point of the part to a varying degree. Example profiles for selected points of the printed part are depicted in Figure 2 and 3. The cyclic nature with reheating periods of decaying amplitude is the most conspicuous characteristic of temperature profiles.

- **Reheating cycles can be determined directly from gcode:** Reoccurring depositions cause cyclic behavior in the temperature profiles. Each reheating period in the temperature profile corresponds to the energy input from the deposition of adjacent roads and layers. Figure 2 designates the deposition time of a heated layer by vertical dashed lines. More importantly, the reheating periods can be pre-computed directly from the gcode (see a series of t_d^i in Figure 2).
- **The amplitude of the reheating periods depends on the distances:** During the first few cycles, each of depositions from the nearest neighborhood initiates a rise in the temperature. Figure 2 shows the trend of the temperature profile for several reheating periods. In this case, the reheating cycles exhibit a decaying amplitude and an increasing time lag between consecutive peaks. Both the amplitude decay and the time lag are consequences of increasing distance from the top surface where heat is applied (from the deposition, or laser). For this process, the number of reheating cycles is finite and small, which is related to the heat transfer resistance of the part and is a function of material properties as well as the geometry of the part.
- **The cyclic reheating pattern persists for various parts:** Figure 3 depicts the temperature profiles of several parts. The temperature profiles have been extracted from simulations of the cuboid-shaped parts at the same location (A), but with increasing part length (as marked in the legend). The increase in part length results in longer time gaps between road and layer depositions that led to the following changes in the profiles:
  - Longer reheating period, due to increased relative deposition time of each layer.
  - Higher temperature amplitude of reheating cycles, due to increased deposition time of each layer and more cooling from top surfaces.
  - Change in the slope of the cooling curve, due to increased distance from cooling surfaces.
  - The average temperature is higher for shorter parts due to a shorter time gap between individual road and layer depositions and associated heat influx from the heat source.

  Nevertheless, the overall temperature profiles remain highly similar. Hence, if the pattern can be captured from simulations of some parts, the temperature can be predicted for other parts as well.
- **Redundancy exists in the temperature profiles:** Figure 4 depicts the temperature profiles for a series of points distributed along a given road. The points are selected from the middle part of the print, away from the boundaries. Note that the temperature profiles are almost identical in the first few reheating cycles. This is an example of redundancy where points exposed to similar thermal conditions have the same cooling pattern.
- **Symmetry exists in the deposition:** Another example of redundancy in the temperature

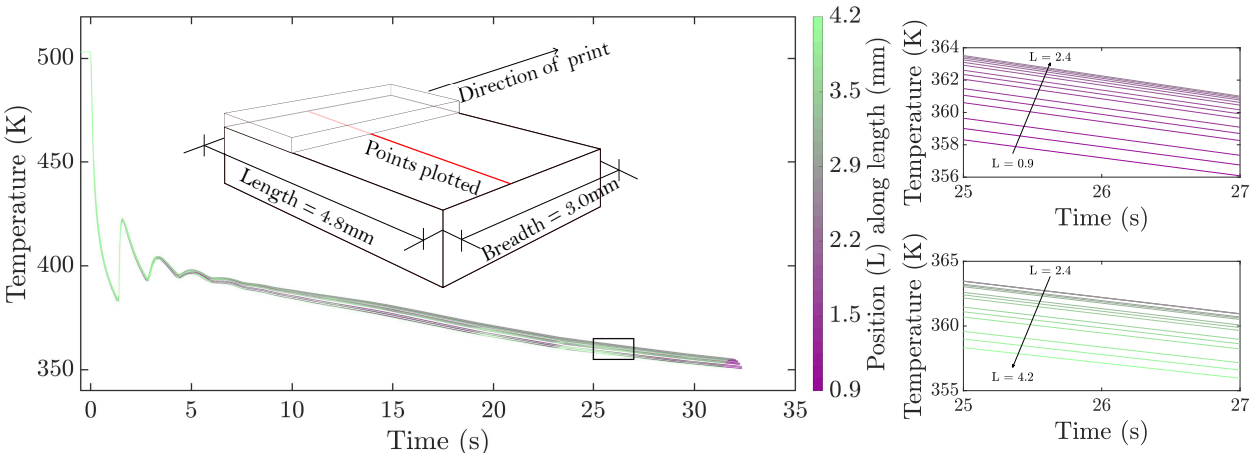

Figure 4: Symmetry in temperature profiles across the print direction. The left panel overlays the temperature profiles of the points along a line perpendicular to the print direction. The line, on which the points are situated, is shown in the schematic diagram in red. The right panels depict separate plots for points on each half of the line. (View in color)

profiles is related to the symmetry in the deposition. Figure 4 depicts the temperature profiles color-coded by the distance along the road. Note that temperature profiles for points close to one end of the road are mirrored with the temperature profile for points from the opposite end of the road. Hence, if symmetry exists in the deposition pattern (not necessarily in geometry), the temperature profiles resemble it.

The occurrence of the above patterns is a direct consequence of an interplay between three heat transfer processes: (i) heat influx into the part from the new depositions at a higher temperature, (ii) heat dissipation from the part into the surroundings due to the convection and radiation from free surfaces, and (iii) heat conduction within the part. Moreover, although the part is three dimensional, the deposition process occurs along one dimension. Hence, we observe that the first order effects from each heat transfer processes can be captured using a set of distances from each heat sink and heat sources. The number of distances required to capture these effects depends on the material used and the process analyzed. In some cases, the number of distances may be relatively high. However, in many cases it is manageable. For FFF, we report that the total number of reheating cycles is as small as four layers and hence manageable. More importantly, we show that it can be determined *a priori* through the calculation of the 'heat influence zone' (HIZ). These are the significant observations for the SM formulated in this paper. There are two additional elements critical to our SM. First of all, we propose to use gcode for the decomposition of the temperature profile. Moreover, we leverage neural networks to quantify the first order (and higher orders) effects as a function of the distance sets determined for each point of the part.

In the next section, we describe three main components of the SM. We first provide a basic introduction to surrogate modeling. Next, we explain the decomposition of temperature profile and the parametrization of the geometry. We also articulate the concept and importance of HIZ for reducing

the complexity of the SM.

3 Surrogate model

'A Surrogate' is a substitute or replacement, which is developed to perform the tasks of the entity it replaces. In the engineering context, a surrogate model (SM) is a statistical model [36, 47], which is designed to produce the response equivalent to the original model at a fraction of the cost without sacrificing accuracy. The significant reduction in the cost is a direct consequence of replacing the underlying governing equation with a function between the selected output and the selected input of the original model. Formally, consider a physics-based model (e.g., numerical simulation) to be a function:

$$y = f(\boldsymbol{x}) \tag{1}$$

where y is the output of the model and $\boldsymbol{x}$ is an array of the input parameters. The corresponding SM is of the form:

$$\bar{y} = \bar{f}(\bar{\boldsymbol{x}}), \quad \bar{\boldsymbol{x}} \in \boldsymbol{x} \tag{2}$$

where $\bar{y}$ is the output of the SM for input parameters $\bar{\boldsymbol{x}}$ and $\bar{f}$ represents the SM. To build SM, $\bar{f}$ must be found by solving an inverse problem [14, 9]. In essence, the focus of SM is first to generate data using the original model, and then to determine the function. Such a model can provide good predictive capabilities at the cost of limiting the explanation for the predicted behavior.

There is no unique way of constructing $\bar{f}$. The most popular SMs can be classified into following families: response surface modeling [20], neural networks [15], kriging [23], and support vector machines [7, 8]. Regardless of the method chosen, designing and building an SM involves four steps [12]:

1. Selection of input and output variables
2. Design of experiments to generate training data
3. Training the SM
4. Validation and testing

The choice of input and output variables delineates the complexity of the model, the number of variables in the model, as well as the number of samples required for training. Such a choice is problem dependent. In the case of this work, the information about the geometry of the part is the desired input, while temperature profile ($T(t)$) is the desired output.

In this work, for any point in the part, we extract a set of distances from cooling surfaces and heat sources using the gcode. We use the concept of HIZ to narrow down the key distances and use them as selected features for the SM. Specifically, we use a small set of distances from heat sources and sinks within the HIZ as the input to the SM model.

The temperature profile is selected as the output variables for our SM. To further simplify the training process, we decompose the temperature profile into reheating periods based on the gcode generated for a given printed part. The motivation for the extra step is grounded in the interplay between different

heat transfer modes active during different reheating periods. During the first period, the temperature cooling profile is affected by a small set of distances from cooling surfaces. For the subsequent periods, the set of distances and their importance changes as more layers are added. Such decomposition allows reduction of the number of input variables and acceleration of the training process of SM.

3.1 Temperature decomposition using gcode

For all points, we transform the temperature profiles from the global time frame (t) to a local time frame ($\bar{t}$) that starts at the deposition time (t_d^0) of the point. The origin of the local time frame is readily available from the gcode. In this sense, the local time frame facilitates the temperature profile alignment to the local deposition. In this local time frame, the deposition time is at $\bar{t} = 0$ for all points.

In Figure 5, the first row depicts the ensemble of temperature profiles for a series of points selected from different parts. Specifically, the first two panels of this figure depict temperature profiles: in the global time frame (t) and in local time frames ($\bar{t}$), respectively. Interestingly, when translated into the local time frame, the pattern in the temperature profiles becomes more prominent.

Next, we decompose the temperature profiles into reheating periods based on the time of subsequent depositions occurring at t_d^i. The second row of Figure 5 depicts the example division of individual curves into constituting five periods (dashed vertical lines added for guidance). Each period corresponds to the time between depositions of the influencing road or layer in the HIZ (e.g., top layer deposition). Such time division into constituting periods can be performed for any point of the printed part directly from the gcode. The temperature profiles in Figure 5 are extracted from the results of a physics-based simulation and demonstrate that proposed decomposition captures the reheating periods accurately.

Formally, the decomposition of the temperature profile $T(t)$ can be expressed as:

$$\bar{T}_{ij}(\bar{t}) = \begin{cases} \left(H\left(t - t_d^{N_j^i}\right) - H\left(t - t_d^{N_j^{i+1}}\right)\right) T_j\left(t\right) \\ \qquad \forall i \in [0, 1, 2, ..., n-1] \\ \left(H\left(t - t_d^{N_j^i}\right) - H\left(t - t^{end}\right)\right) T_j\left(t\right) \\ \qquad i = n \end{cases} \tag{3}$$

where $T_j(t)$ is the temperature profile at the j^{th} point, $H(\cdot)$ is the Heaviside function, and $\bar{T}_{ij}(\bar{t})$ is the i^{th} segment of that temperature profile. This is shown in panel (b) of Figure 5. Index N_j^i is the i^{th} influencing deposition on the j^{th} point. The last period of the temperature profile extends to the end of the simulation(t^{end}). The time for subsequent deposition $t_d^{N_j^{i+1}}$ and the number of influencing deposition are location specific and depend on the part geometry, deposition pattern, and deposition speed.

The decomposed temperature profiles are mapped into an m dimensional space by fitting them with a curve. The type of the fitting curve is chosen based on the thermal behavior and ease of representation. The first period exhibits exponential cooling and hence an exponential function is more suitable. All

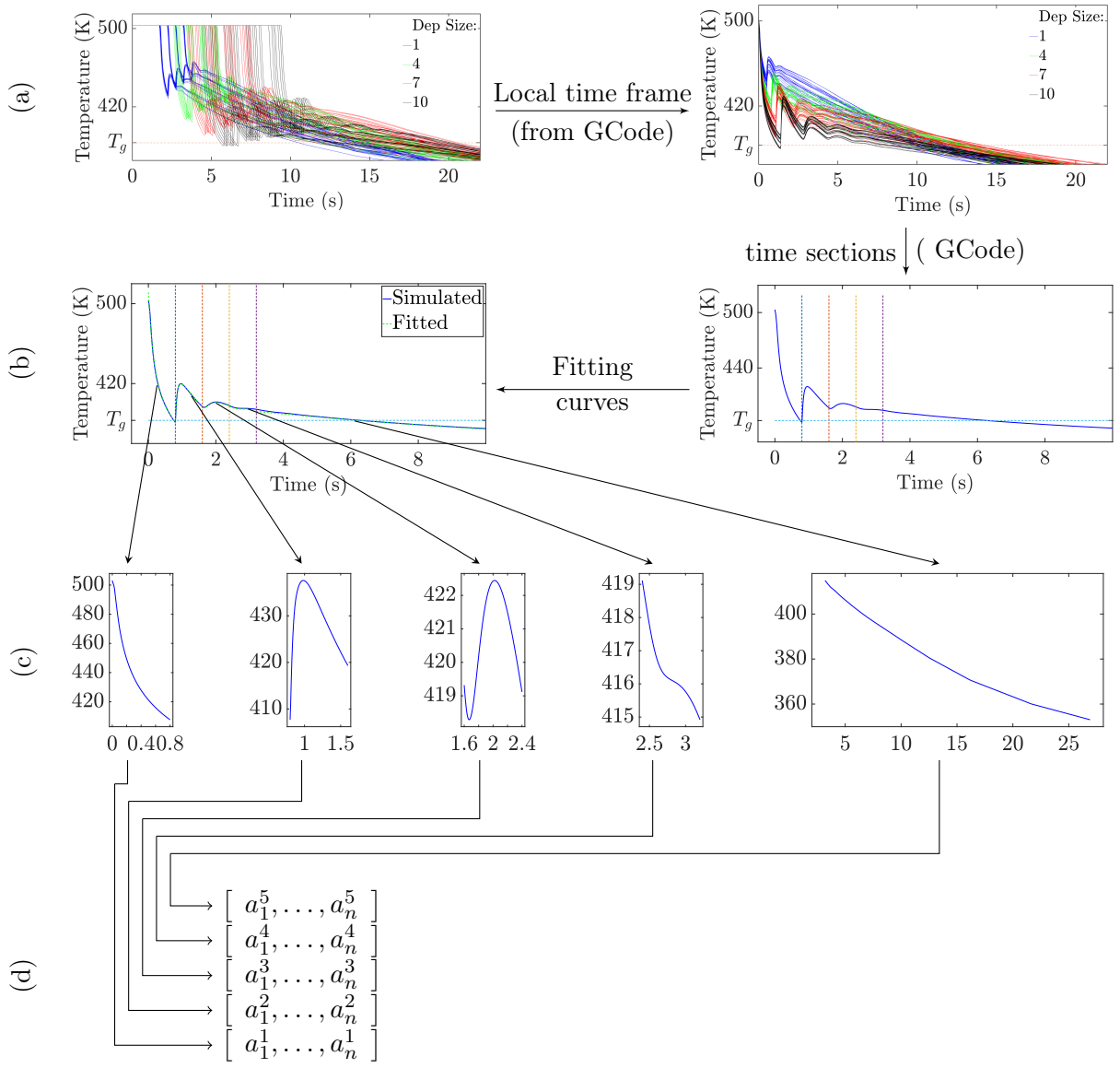

Figure 5: Basic steps involved in decomposition of temperature profile and curve parametrization. (a) Temperature profiles, (b) slicing and fitting, (c) decomposed temperature profiles, and (d) training.

other periods follow an exponential heating and then cooling pattern. In principle, all the periods can be represented using an exponential function, but polynomial functions exhibit better training performance for some periods. We attribute the poor performance of exponential functions to the small time lag between the deposition time used for temperature decomposition and the time of actual initiation of the reheating. The time lag is small and can be estimated or trained with more data, but for the process considered in this work, it has a small effect on the overall thermal behavior, while significantly affecting the training performance. The temperature profiles are fitted as follows:

$$\bar{T}_{ij}(\bar{t}) = \begin{cases} a_1^i e^{a_2^i t} + a_3^i e^{a_4^i t} & \forall i \leq 2 \\ \sum_{k=0}^{3} \hat{a}_k^i t^k & \forall i > 2 \end{cases} \tag{4}$$

where a_k^i and $\hat{a}_k^i$ are the k^{th} coefficient of the fitted curve representing the i^{th} period of the temperature profile. Regardless of the choice of the fitting function, the SM seeks to map the regression coefficients for the corresponding basis functions with the set of local distances from heat sinks (cooling surfaces) and heat sources (moving heat source and deposition of new materials).

The temperature is decomposed into n periods. The number of periods, n, is dependent on the total number of influential depositions that are determined using HIZ – discussed in the Appendix. Example time decomposition is shown in Figure 5 (third row). Note that the number of reheating periods for these profiles is small. The temperature profiles have at most five periods where some of them exhibit clear cooling behavior and the rest of them show reheating behavior.

3.2 Feature selection

The efficiency of the training process of an SM and its performance heavily depends on the selected feature set. A well-designed set of features leads to faster learning and more accurate predictions.

The feature set can be constructed from the raw data through statistical methods (e.g., wrapper methods [22], filter methods [16]). These methods do not consider the underlying physical process, and hence, are useful when the process is complex or unknown. In this work, we adopt a different approach. We take the physical characteristics of the deposition process to guide the feature selection for the SM.

Features directly linked to heat influence zone

We define a zone over which any heated deposition has a significant effect. The zone is dependent on the material properties and the process parameters. For a given material and a specific printing process setup, it is possible to identify the maximum extent of the zone; that we call the Heat Influence Zone (HIZ). It is essentially the maximum distance from a heat source/sink where a minimum observable thermal change occurs. The size of HIZ guides the design of input parameters (features) for the SM. In this sense, the size of HIZ is critical to parameterize the coefficients of the curves for individual reheating periods. HIZ corresponds to the spatial region where the first order effects are dominant, and distances within this zone must be included as an input for the SM. The contributions from heat sources/sinks outside of this zone may be of less influence and hence can be ignored.

To estimate the size of HIZ, we leverage the analytical solution to the transient heat equation with a point source on a semi-infinite body [35]. Figure 6 depicts the characteristic feature of HIZ determination, while details of the analytical solution are given in the Appendix of this paper. The analytical model is leveraged to determine the temperature profile due to deposition of a heated layer. As the layer is deposited the temperature in the neighborhood increases. The heat from the deposited layer dissipates through the system and increases the temperature of the specimen. Over time, the heat traverses to the lower layers while the top layers cool down, as shown in the figure. Figure 6 depicts the time evolution of temperature change ($\Delta T = T - T_0$) as a function of distance from the heat source at the center of the sample. The results are obtained using the solution from Equation 17. The temperature is computed for a part with height corresponding to twenty layers at an initial temperature of $T_0 = 25$ ℃. One heated layer with 20 roads (*each road* $4mm \times 0.2mm$) is deposited over twenty layers at an initial temperature of 210 ℃. The cooling effect due to convection and radiation is ignored. The choice on the geometry allows a conservative assessment of the thermal behavior of the representative points in the printed part and thus, leads to a conservative estimate of the HIZ.

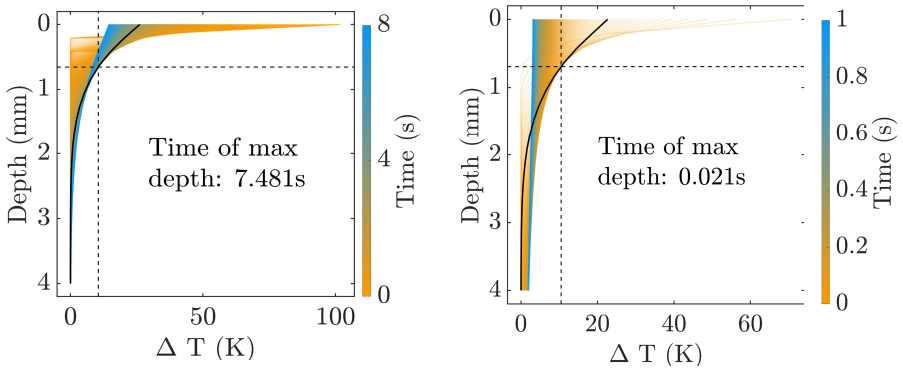

(a) ABS Plastic (b) CF-PLA Plastic

Figure 6: Heat penetration for (a) ABS and (b) Carbon fiber PLA due to a heated deposition.

Figure 6 depicts the temperature evolution for two materials: ABS and CF-PLA. In each case, the HIZ is estimated and marked based on the following criteria. For a point to be considered inside the HIZ, a minimum increment in temperature must be observed. This threshold considered in this work is set as 10% of the glass temperature (105 ℃) of ABS. Such criteria mean that for a point to be in the HIZ of a deposition the rise in temperature must be at least 10.5 ℃. The maximum depth at which the minimum temperature change by 10.5 ℃ is approximately 0.8 mm for ABS plastics (Figure 6, left panel). For CF-PLA (right panel) it is approximately the same. The major difference between these two materials lies in the time when the heat penetrates the material. For ABS, it is at approximately 14 s and for CF-PLA it is at approximately 0.03s. The shorter time occurs due to the higher conductivity of the carbon fibers in CF-PLA.

The estimation of the HIZ translates to approximately four layers for the ABS in FFF printing process. Hence, for any point in the printed part, the maximum number of layers for which a significant temperature is expected is four, assuming the filament thickness to be 0.2 mm. This estimation agrees well with the representative cooling curves in Figure 2. The temperature profile is characterized by

four cyclic reheating periods. Moreover, it remains unaffected by the subsequent depositions beyond the fourth layer. Hence, it is concluded that any deposition beyond the estimated size of HIZ has a negligible effect on the temperature profile.

Once the size of HIZ is estimated, for any point of interest in the part, a set of distances from cooling surfaces and heat depositions is determined. Rather than using the spatial coordinates (x, y, z) of a given point, their contribution towards the thermal properties is quantified by the set of relative distances (d_c^k) from the cooling surfaces. The set of distances is guided by the gcode and HIZ. If the surface is within the HIZ, the corresponding distance is taken as an input to the SM. In practice, three types of information are determined: (i) the deposition time of the influencing depositions (t_d^i), (ii) the corresponding distance (h_d^i) to the heat source, and (iii) the distance (d_c^k) from the cooling surfaces. The set of distances is location specific.

3.3 Output construction

With the input variables (features) defined, we now introduce the protocol for output construction. In general, for any point of the part, we seek to determine the map between the input parameters (features) and the temperature profile. The temperature profiles are considered as a function of the two types of features: (i) features defining the part geometry (d_c^k, A_c^k) and (ii) the features related to deposition pattern (h_d^i, t_d^i):

$$T = f(d_c^k, A_c^k, h_d^i, t_d^i, t). \tag{5}$$

The final step is to reconstruct the full temperature profile from the constituting segments while ensuring continuity:

$$T_j(\bar{t}) = \sum_{i=0}^{n-1} \Big(H\big(t - t_d^i\big) - H\big(t - t_d^{i+1}\big) \Big) T_{ij}\big(\bar{t}\big) + \Big(H\big(t - t_d^{n-1}\big) - H\big(t - t_j^g\big) \Big) T_{nj}\big(\bar{t}\big) \tag{6}$$

where t is the time, $T_{ij}(\bar{t})$ is the temperature profile of the j-th point at the i-th period, and $\bar{t}_d^i$ and $\bar{t}_d^{i+1}$ are the time of i-th and $(i+1)$-th nearest influencing deposition, respectively. Time t_j^d is the time of deposition of the j^{th} node and t_j^g is the end time of modeling where consolidation stops. It defined as,

$$t_j^g = \underset{t}{\operatorname{argmax}} \left(T_j(t) \geqslant T_g \right) \tag{7}$$

where T_g is the glass temperature of the material.

3.4 Training

The training of the SM is done using a set of artificial neural networks. Each period of the temperature profile is trained by a separate neural network. It is motivated by the dynamics of the deposition process and the associated change in the set of distances from heat sinks and sources. Moreover, by decomposing the temperature profile, less data is required for training.

For the same reason, we introduce three categories of points: top points (on the top surface of the road), side points (on the side surface) and corner points. Each category is trained separately as they exhibit different cooling regime. The points in the top of the deposited material are affected more by the deposition of top layers, while the points on the side are more influenced by the road right next to it. The points in the corner have characteristics of both. A schematic for the SM with the structure of the neural network is shown in Figure 7.

We notice that the general trends should be captured without introducing these categories; however, it would require a much larger data set for training. In principle, it is possible to generate data for any resolution; however, the required time for data generation and training prohibits a significant increase in the resolution.

In summary, for HIZ of four layers, the temperature profile is divided into five periods. With three categories of data points, in total fifteen neural networks are constructed and trained to predict the temperature profile. This type of data division and model formulation is known as context-aware learning [6].

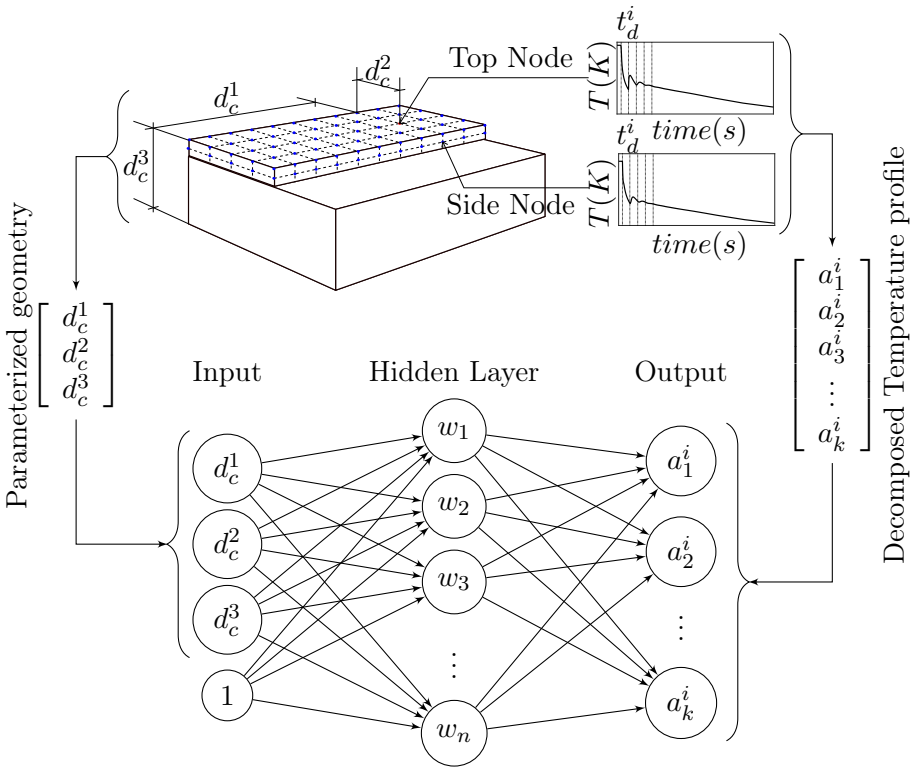

Figure 7: Structure of the surrogate model.

4 Results

We choose the fused filament fabrication process to showcase the capabilities of the surrogate model. FFF is an additive manufacturing process that fabricates prototypes by depositing layers of semi-molten thermoplastics. The material is deposited through a heated extruder that is controlled by a gantry machine. The extruded thermoplastic cools down and fuses with the surrounding material at the high temperature. The formation of the bond between two thermoplastic surfaces at a high temperature is induced by polymer diffusion. The details of the physical, mathematical, and computational model are provided in details in the Appendix.

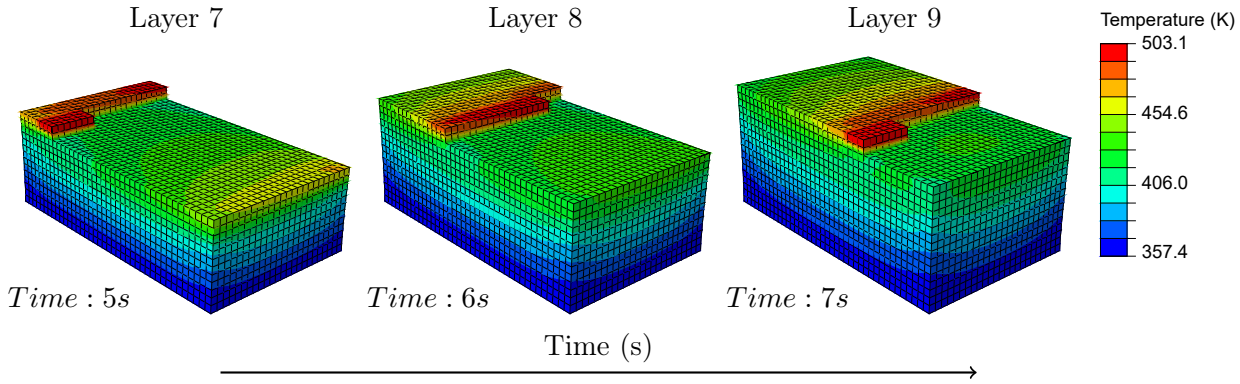

Figure 8: Temperature distribution in the gradual deposition process at selected point in time.

4.1 Data generation

As in any data-driven approach, the accuracy of SM is mostly dependent on the data used to build that model. In particular, the sampling of the input space directly affects the accuracy of the model. The data generated for the training step must cover the domain of interest uniformly. Standard sampling strategies include methods such as Latin hypercube sampling [37, 57, 39, 24, 48, 21], or orthogonal arrays being part of design of experiments [29, 31]. These methods can be directly applied to problems where input variables are independent, which is not the case for this work. In this work, sampling of the SM input space is directly connected with the part geometry.

For simplicity, we choose a cuboid shape as shown in Figure 8 in the Appendix. The aim of this work is to prove the concept, and we first focus on the effect of size rather than the geometry of the part. For that reason, we establish the SM which can predict the temperature profile for different sizes of a single shaped geometry.

In total, eleven parts are considered. The width and the height of the cuboid are kept constant at 2.4 mm and the length is varied from 2 mm to 6 mm (three times increment). Results from FEM are processed to extract the temperature profiles. The generated data is divided into two categories: training data set and testing data set. The training data set contains the temperature profiles for the

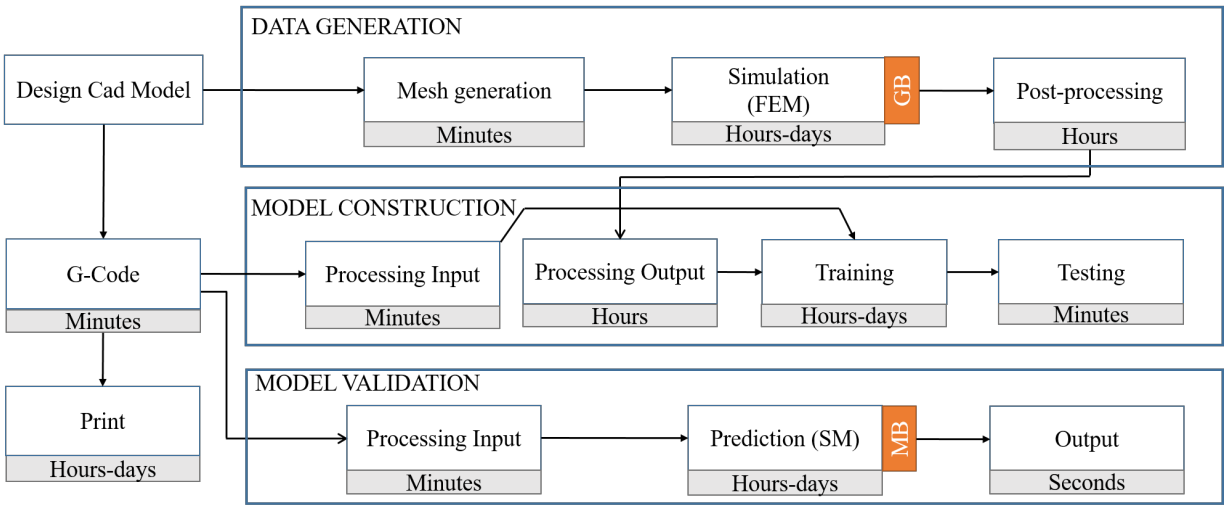

Figure 9: Workflow of surrogate model construction with the approximated time and storage required to complete individual steps.

parts with mid-range of length: 3.2, 3.6, 4.4, 4.8, and 5.2 mm, as described in Table 1. All together the training data set consists of 26,000 data points for surface (top and side) nodes, each point being one temperature profile ($T(t)$). The testing data set contains the temperature profiles for part-lengths: 2.0, 2.4, 2.8, 4.0, 5.6, and 6.0 mm. The part dimensions considered in this work are consistent with many state-of-the-art computational models [58, 53]. The largest part (L = 6.0 mm) consists of 12 layers (0.2 mm thick), each layer is made up of 15 roads (0.4 mm wide) of 2.4 mm length. Each road is divided into 24 unit depositions. Hence, the part is made up of 4320 discrete depositions.

This choice of the data-set division allows testing the SM in two scenarios: interpolation and extrapolation. In the interpolation scenario, we aim to test the robustness of SM to predict the temperature profile for the part that is within the range of length used in training (3.2-5.2 mm). Specifically, we choose the part of the length of 4.0 mm. In the extrapolation scenario, we choose data sets that are generated outside the length range used in training. Specifically, we choose the part length of 2.0, 2.4, 2.8, 5.6, and 6.0 mm. These parts are at both ends of the length spectrum creating an excellent opportunity to evaluate the robustness of the SM.

The physics-based simulations are performed using ABAQUS®. The details regarding the simulation are summarized in the Appendix. The FE simulations and data extraction were conducted on a 12 CPU system (Intel® Xeon® E5645 @2.40 GHz with 48GB RAM).

4.2 Training and validation

The neural networks comprising the SM are trained using the data from the FEM simulations. Figure 9 describes the work-flow to train the SM. The control parameters (optimization function, number of hidden layers, convergence criteria) of these neural networks are selected such that the error in the

output is minimized. The SM testing is done on a single CPU (Intel® Xeon® E5645 @2.40 GHz with 48GB RAM) in serial.

The output of the SM is a temperature field which is divided and fitted according to section 3.3. The coefficients of the fitted temperature profiles are the output variables of the neural network. Following are the details of the neural network parameters:

- Type: Single layer shallow NN (Figure 7).
- Training Function: Bayesian regularization with back-propagation.
- Number of hidden nodes: Varies $(6 - 40)$
- Target training error: 10^{-5}

The parameters are set to accommodate faster convergence in training and to avoid over-fitting. The training function determines the regularization factor to reduce over-fitting. A large regularization factor may learn more generalized trend but may cause underfitting. A lower value of the regularization factor may lead to over-fitting causing the model to behave poorly for new data sets. From Figure 10, we can observe that the training of the NN has no trace of over-fitting as the testing error is following the trend of the training error.

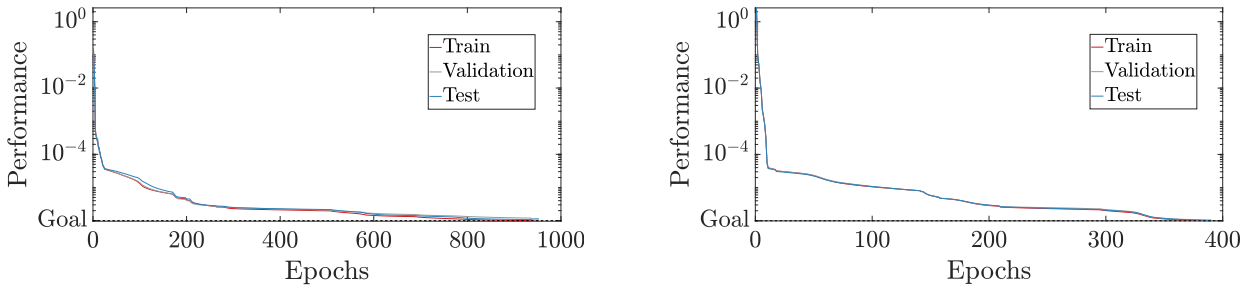

Figure 10: Performance plot of the neural networks for section 1 and section 3 of the temperature profile. The 'Goal' is to achieve a training error less than or equal to 10^{-5}.

4.3 Testing

The aim for constructing the SM, described in the Section 3 and Section 4.2, is to predict the thermal behavior of the printed parts. As the first step to verify the robustness, we evaluate its ability to predict the thermal profiles for a few testing data sets.

We present the comparison between the FEM and SM by focusing on two essential qualities of computational models: accuracy and speed. Accuracy provides the quantitative measure at which the SM can predict the thermal outcome compared to the FEM (Figure 11, 12, 13, 14, 15, and 16). We assess the accuracy of the SM by comparing two aspects: temperature profile in time and temperature distribution in space. Firstly, we present the error of SM for a few selected points in space (Figure 11

and 12). Next, we present the spatial accuracy of the SM at a few selected points in time (Figure 13, 14, 15, and 16). We report the errors for both extrapolation (Figure 15 and 16) and interpolation scenario (Figure 13 and 14). Finally, in Figure 17 we report the error for all points in the parts. We close this section by comparing the computational time of both models in Table 1 as computational speed is the major motivation for creating the SM.

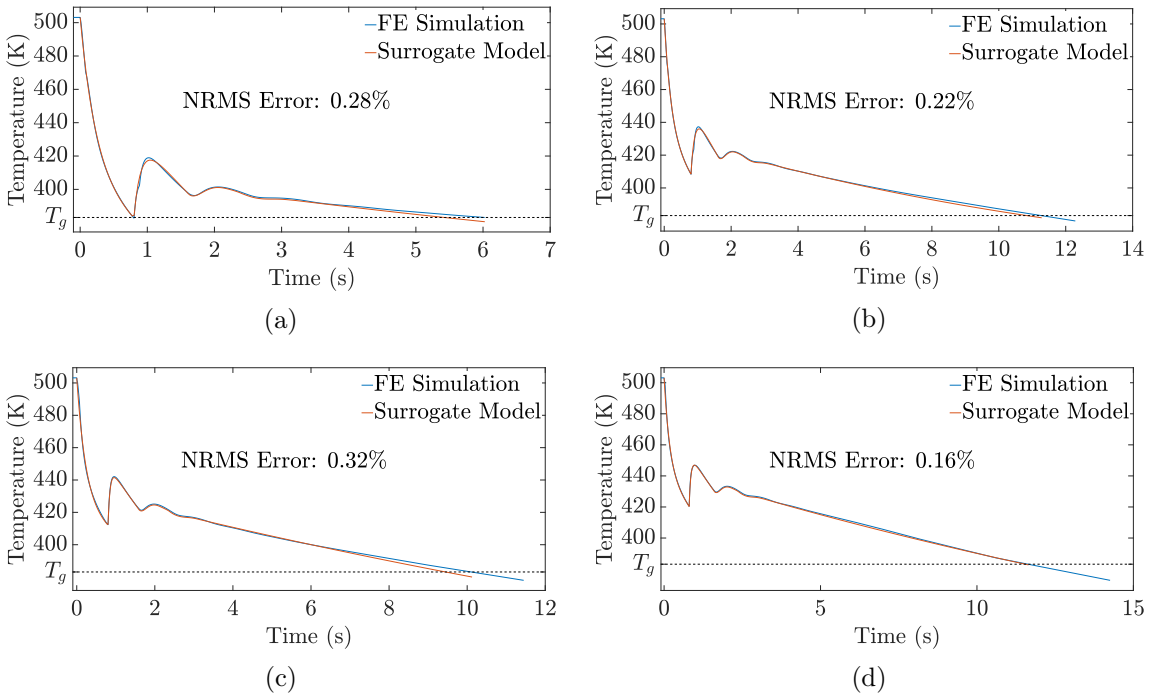

Figure 11: Temperature profiles for selected points predicted using FEM and SM for the **interpolation scenario** (L = 4 mm). Note: The representative points are chosen at different layers, (a) layer 2, (b) layer 4, (c) layer 5, and (d) layer 6.

Figure 11 depicts the temperature profiles ($T(t)$) for a few selected points. These results correspond to the **interpolation scenario** (print of length 4 mm). Each panel depicts $T(t)$ from FEM and overlays it with the same from the SM. The four points are representative of different layers in the printed part. In each case, the temperature profiles show the characteristic cyclic reheating. The results show good correspondence between the temperature profile from the SM and that from the FEM. In each case, the error in the temperature prediction is below 2%. The representative points in Figure 11 have error of 0.28, 0.22, 0.32, and 0.16%, respectively. The error is quantified by the Normalized Root Mean Square Error (NRMSE) defined as:

$$NRMSE = \left(\frac{1}{t_{end}} \int_0^{t_{end}} \left(\frac{T_{FEM}(t) - T_{SM}(t)}{T_{FEM}(t)} \right)^2 dt \right)^{1/2} \times 100\ \% \tag{8}$$

There are a few characteristics worth articulating:

- The deviation of the SM predictions from the FE profiles is low in all sections.
- The peaks obtained by the SM lines up with that of FEM with satisfactory accuracy.
- The SM is designed to only maintain C^0 continuity in time at the intersection of each section. To ensure this temporal continuity, the start of each cycle is superposed with the end of the previous one, which may potentially cause error propagation. However, its effect is minimal.

Similar to Figure 11, Figure 12 shows the temperature profiles of the **extrapolating length** (5.6 mm) for four representative points at different layers. The results from the SM show acceptable correspondence with the results from the FEM. The error found at these points are 0.57, 0.30, 0.38, and 0.64%, respectively. The associated error is slightly higher than that of interpolation scenario. However, it is well within the tolerable limit (5%). Moreover, in this scenario, the print size is longer than the parts used for the SM training. In particular, the length is increased by 7%, but the measured error is still below 2%. We further increase the print length up to 15% ($L = 6\ mm$) and the mean error was found to be 1.84%. Although further increment of print length is possible, it is restricted by the substantial time and storage space required by the FEM simulation. Nevertheless, our results clearly demonstrate the robustness for both interpolation and extrapolation scenario of the SM.

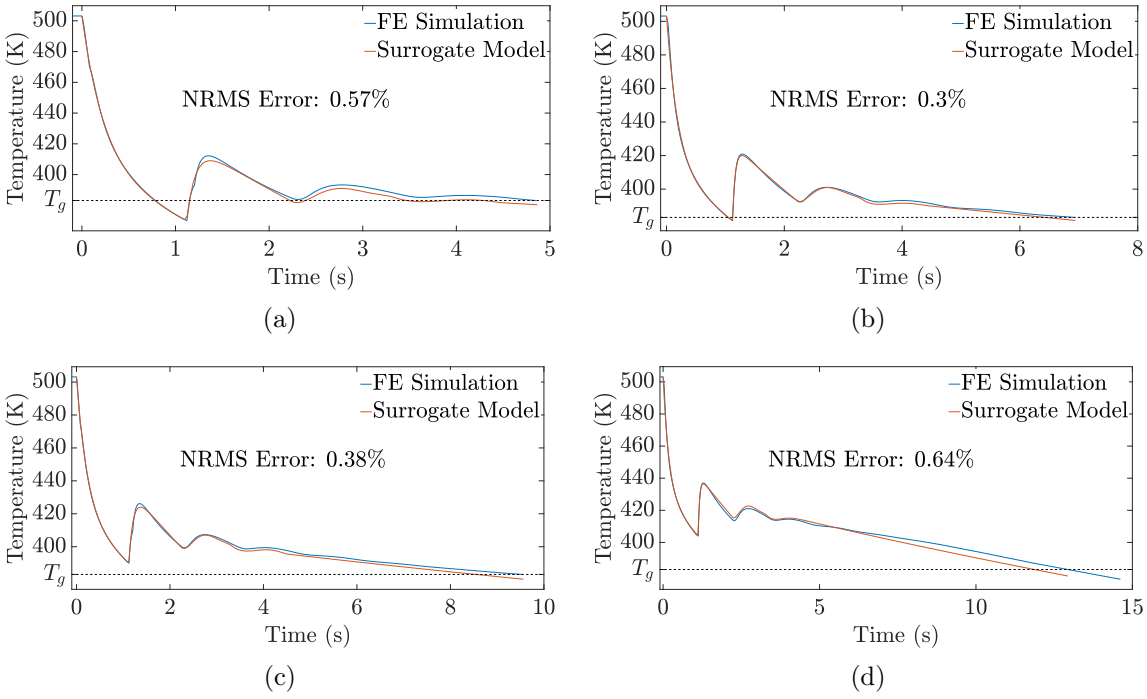

Figure 12: Surrogate model predictions and FE simulation results for the **extrapolation scenario** (L = 5.6 mm). Note: The representative points are chosen at different layers, (a) layer 2, (b) layer 3, (c) layer 4, and (d) layer 6.

We also compare the results for the spatial temperature distribution at selected points in time. Figure 13 depicts the comparison of FEM and SM for the **interpolation scenario** (L = 4.0 mm). The

temperature distribution on the layer 5 from the FEM in panels (a, b, c, d) and from the SM in the panels (e, f, g, h) is compared. The relative error is also presented in the panels (i, j, k, l) of this figure. In the first row of each column, a schematic diagram of the printed part is shown for each the corresponding time. In these diagrams, the cross-section of the layer in focus (layer 5) is marked by arrows. The second row of the figure presents the temperature distribution from the FE simulation. The third row depicts the temperature distribution from the SM and the last row provides the relative error distribution. Each column represents a different time in the printing process. The first column results from the time t_1 when the fifth layer is completely deposited. From the temperature distributions, we observe a gradient in temperature along the breadth (lower temperature near the bottom and higher temperature near the top) forms. As the roads are being deposited along the breadth, as shown in Figure 4, higher temperature and higher temperature gradients form. In both cases, the depositions near the start of length have a lower temperature than the relatively recent depositions near the end, since they get more time to cool down. Also, we see a higher temperature near the center and the boundaries are at a lower temperature. The effect of higher surface cooling at the boundaries causes this behavior. The set of temperature distribution illustrates these key characteristics of thermal processes occurring during layer by layer deposition. Our SM is capturing well all these transient characteristics while mimicking results from FEM with good accuracy.

Similar observations are made for second and third column of the figure that represents the time t_2. At this point, the layer 6 is completely deposited over layer 5. The newly deposited layer causes a temperature rise in the bottom layer. As mentioned earlier, due to the effects of convection and radiation on the boundaries, a higher temperature is retained at the center. In this time frame, all the points on the surface are at the first reheating cycle of their temperature profiles. In the third column of Figure 13, the next layer is half deposited and it causes a rise in the left half of the print, which is apparent in both FEM and SM distributions. Hence the left half of the print is in the second reheating cycle of their thermal profiles. At the last column of Figure 13, another layer is half deposited, but due to its higher distance from layer 5, the reheating effect is less pronounced.

All these results show good conformity between SM and the FEM. The maximum error is found to be less than 1.5%. The error distribution is random as a general nature of the ANN used in the SM. There are a few notable observations as follows:

- The SM predicts the spatial pattern in the thermal behavior that is in line with the finite element model.
- Although no provisions are made for spatial continuity, the discontinuity is well within tolerable limit.

Figure 14, depicts a temperature distribution comparison for layer 7 of the same **interpolation case** (L = 4.0 mm). Here, at time t_1 the layer 7 is deposited completely and at t_2 layer 8 is completely deposited over it. Similar trend in temperature distribution are observed for layer 5 in Figure 13. Since this layer is further from the base, the cooling effect of the base is significantly reduced and hence the overall temperature is higher. These results further assert the predictive ability of the SM with respect to the interpolation scenario.

Similar observations are drawn from other test parts. In Figure 15 and 16, we present the spatial

distribution of temperature of the **extrapolation scenarios** (L = 5.6 mm). The layout of the panels are same as in to the previous figures, we focus on layer 5 (Figure 15) and layer 7 (Figure 16). Each column depicts temperature distribution for a selected point in time in the printing process. Again, the first row consists of the schematic diagram of the print at the selected time with the concerned section marked with arrows. The second and third rows provide the thermal distributions from the FEM and SM respectively. The third row depicts the error in the SM. For Figure 15, the first column corresponds to the time when the fifth layer is fully deposited and in the second column the temperature distribution is shown when another layer is deposited over it. The seventh layer is half deposited at the third column and it is apparent from the rise in temperature in the left half of the layer. In the fourth column, the eighth layer is half deposited. In all cases, there is a good correspondence between the FEM and the SM and the error is within 1%.

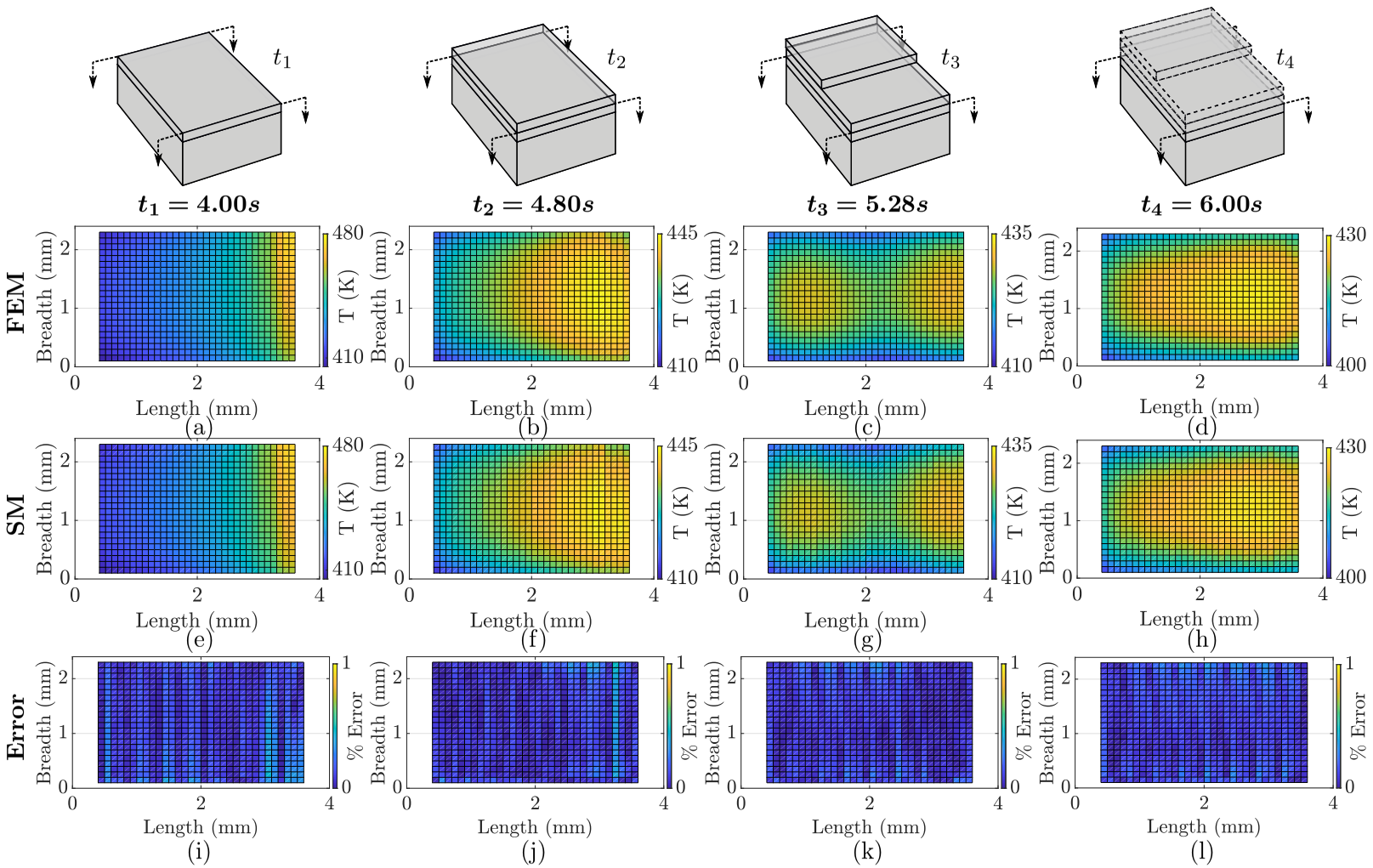

Figure 13: Temperature distribution at **layer 5** for the **interpolation scenario**. Panels a,b,c,d depicts the results from the FEM. Panels e,f,g,h are predictions from our using the SM. Panels i,j,k,l depicts the error in the predicted temperature distributions. Each column depicts a different time in print. At time t_1 Layer 5 is completely deposited. At time t_2 is the time one more layer is deposited over Layer 5. Similarly, at t_3 and t_4 a second layer and a third layer is half deposited respectively.

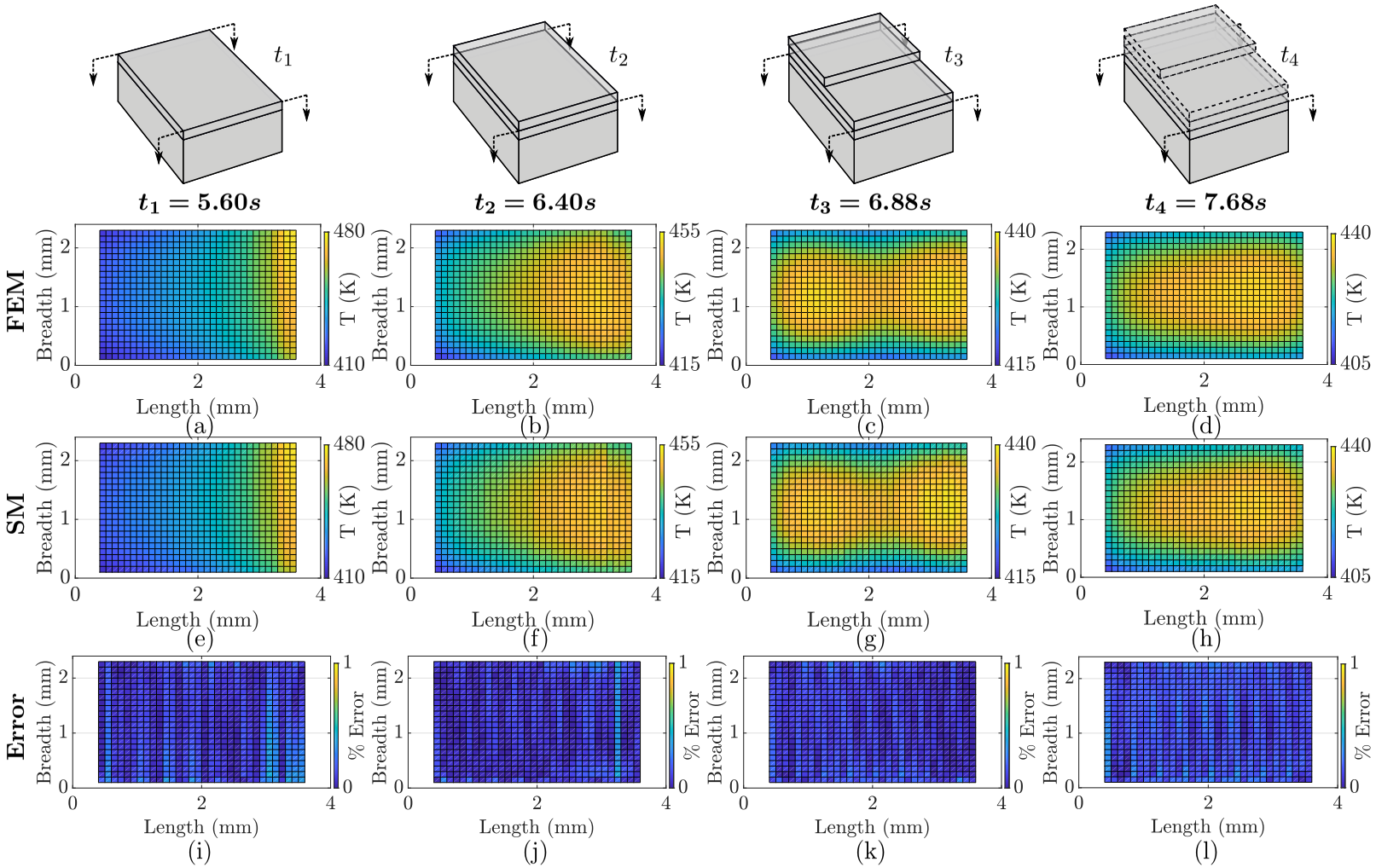

Figure 14: Temperature distribution at **layer 7** for the **interpolation scenario**. Panels a,b,c,d depicts the results from the FEM. Panels e,f,g,h are predictions from our using the SM. Panels i,j,k,l depicts the error in the predicted temperature distributions. Each column depicts a different time in print. At time t_1 Layer 7 is completely deposited. At time t_2 is the time one more layer is deposited over Layer 7. Similarly, at t_3 and t_4 a second layer and a third layer is half deposited respectively.

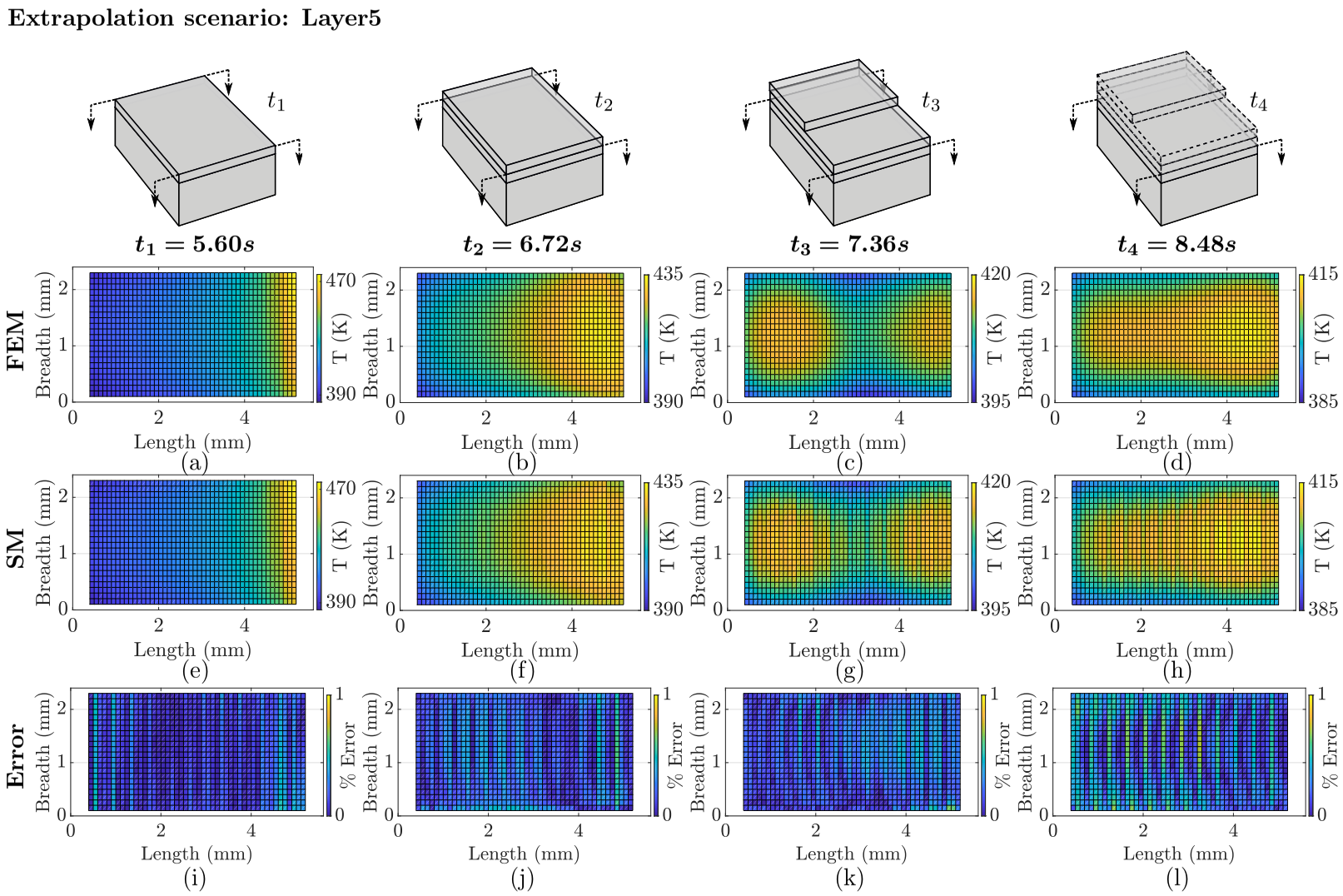

Figure 15: Temperature distribution at **layer 5** for the **extrapolation scenario**. Panels a,b,c,d depicts the results from the FEM. Panels e,f,g,h are predictions from our using the SM. Panels i,j,k,l depicts the error in the predicted temperature distributions. Each column depicts a different time in print. At time t_1 Layer 5 is completely deposited. At time t_2 is the time one more layer is deposited over Layer 5. Similarly, at t_3 and t_4 a second layer and a third layer is half deposited respectively.

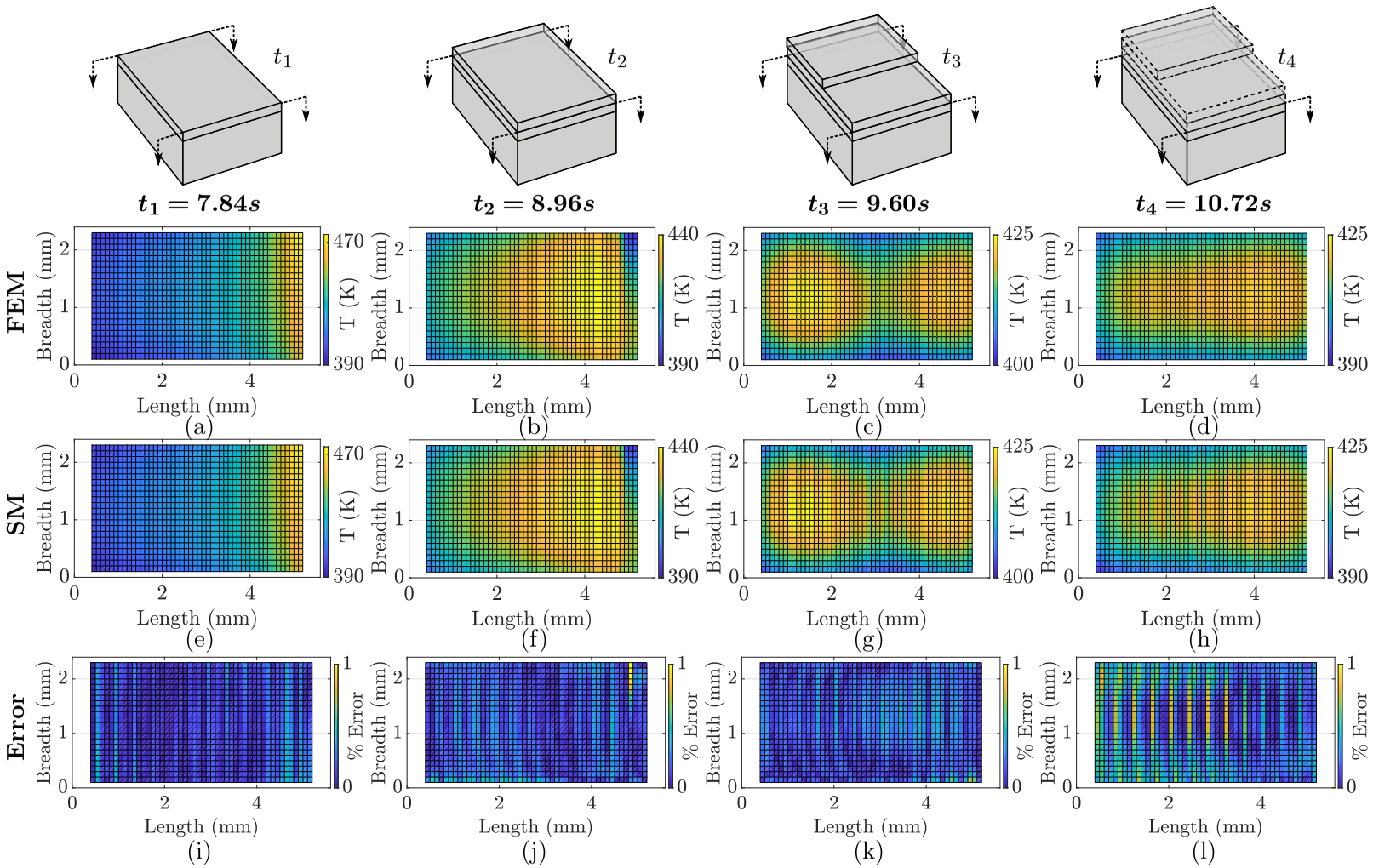

Figure 16: Temperature distribution at **layer 7** for the **extrapolation scenario**. Panels a,b,c,d depicts the results from the FEM. Panels e,f,g,h are predictions from our using the SM. Panels i,j,k,l depicts the error in the predicted temperature distributions. Each column depicts a different time in print. At time t_1 Layer 7 is completely deposited. At time t_2 is the time one more layer is deposited over Layer 7. Similarly, at t_3 and t_4 a second layer and a third layer is half deposited respectively.

To collective assert the error of the SM predictions, Figure 17 shows the cumulative variation of NRMS error in the temperature profile predictions between SM and FEM for the top surface points in the entire part. The panel (a) depicts the error distribution for the interpolation scenario. Each section in this figure, denoted by a dashed line, corresponds to a layer of the print and is designated by 'L'. Our results demonstrate that the error for all points is less than 2%. The error is smaller in the first two layers (less than 1%) and it gradually increases till the fifth layer. However, it is still less than 2%. The error reaches its maximum value at layer five and does not increase in the subsequent layers. The first layer is excluded from both training and testing as it is adjacent to the base and behaves differently than other layers due to base cooling. We observe similar behavior for the extrapolation scenario that is summarized in panel (b) of Figure 17. In this scenario, the error stabilizes at layer six and it is always within 2%. Similarly, we also observe a lower error in the bottom few layers.

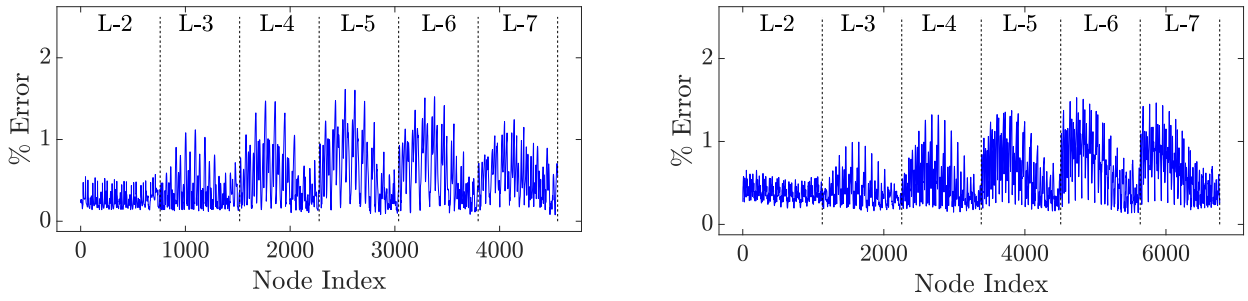

(a) Interpolation scenario: Print size 4.0 *mm*

(b) Extrapolation scenario: Print size 5.6 *mm*

Figure 17: Error in the surrogate model predictions for the top surface nodes in the printed parts for layers L2-L7 (the second layer to the seventh layer).

We close the results section by discussing the computational cost and gains of SM. Specifically, Table 1 provides the details of the computation time and memory requirements for the SM and their comparison with the FEM. The first column reports the length of the simulated parts. As discussed earlier, the width and height of the samples are kept constant at 2.4 mm and the length is varied from 2.0 mm to 6.0 mm at an increment of one road width (0.4 mm). The first three and the last two samples, marked by red boxes, are extrapolation testing data sets and are not used in the training of the SM. The print size 4.0 mm, marked by a blue box, is used as the interpolation testing data set. The degrees of freedom (DoF) reported in the second column corresponds to the number of grid points in the simulation of FEM.

The time required to obtain a thermal history using SM and FEM is reported in the Execution Time column. The Extraction Time reported in the table is the time required to extract the thermal profiles from ABAQUS® object files. The execution time for the FEM increases exponentially with the DoF (from 2.5 to 35 hrs), as presented in the second column of the table. This is a signature of gradual deposition and mesh activation. Although various techniques can be used to reduce the computation cost, the custom models suffer from this computational burden. This is in contrast to the execution time for SM which is linear with respect to DoF. This is expected, since the SM has capabilities of determining the thermal behavior of any point solely based on the set of local distance within HIZ and without coupling it to the behavior of the entire part. The average time required to construct a single

temperature profile T(t) by the SM for a single point is $0.036s$, which opens the avenues for real-time predictions, in-situ controls, and process optimization.

The input and output data size required by both FEM and SM is compared in the columns of Data Size. The input for FEM is the input file ('.inp' file) and subroutines required by the software to perform the analysis. For the SM the reported data size corresponds to the input parameters. Interestingly, the input data required for the FEM and SM are of comparable size. However, the output storage requirement for the FEM is three orders of magnitude higher than that of the SM. The small memory and processing requirements of the SM enables it to be implemented in small single-board computers (e.g. raspberry pi).

The error of the temperature response derived from the SM model is reported in the Average Error column which is the most important factor determining the merit of the SM. The reported errors are NRMSE defined in Equation 8. Nevertheless, the recorded mean error is less than 5% as seen in the Mean column. From the column, we observe that the extrapolation error are larger than for interpolation scenario, which is expected.

In summary, our SM is systematically evaluated based on its accuracy and execution time. Our SM predicts the thermal behavior with high accuracy (error$<$5%) in almost real time. The low storage requirement is a clear benefit which aids towards its implementation on the CPUs of cheap printers.

Table 1: Time and storage space requirements

Length (mm)	Degrees of freedom	Execution Time			Data size				Average Error	
		FEM (hr)	Extract T (hr)	SM (s)	Input (MB)		Output			
					FEM	SM	FEM(GB)	SM(KB)	Mean	Std
2.0	13125	2.5	1.0	81.5	1.92	0.17	0.71		1.61	0.77
2.4	15625	3.5	1.5	106.1	2.33	0.23	1.0		1.02	0.38
2.8	18125	5.5	2.0	127.0	2.74	0.28	1.36		0.70	0.21
3.2	20625	7.0	2.5	140.5	3.15	0.33	1.77		-	-
3.6	23125	9.5	3.5	164.2	3.56	0.39	2.23		-	-
4.0	25625	12.0	5.0	185.8	3.97	0.44	2.75	794.11 KB	0.73	0.29
4.4	28125	16.0	6.0	205.9	4.38	0.49	3.32		-	-
4.8	30625	19.5	8.0	234.2	4.79	0.55	3.94		-	-
5.2	33125	26.0	10.0	251.6	5.20	0.60	4.62		-	-
5.6	35625	30.5	12.0	280.8	5.67	0.65	5.35		1.13	0.38
6.0	38125	35.5	14.0	325.9	6.03	0.71	6.14		1.84	0.86

Notes: Red boxes are extrapolation and the blue box is interpolation data set. The unmarked data sets are used for training the surrogate model. (view in color)

5 Conclusions and Future work

In this paper, we have proposed, developed, and tested the SM capable of predicting the thermal behavior of an example thermally driven additive manufacturing process. We used the FFF process to showcase our approach. The SM was built using the data from a physics-based model. It predicts the thermal profiles for the testing data sets with high accuracy (>95%) in a fraction of time (1000 times faster compared to the physics-based model). The model was created to generate the thermal profiles for different sizes of the same geometry and was tested for both interpolation and extrapolation scenarios. In both cases, we observed exceptional accuracy at a low computation cost. The storage space and computational power required for the ANN-based SM are extremely low compared to a FEM. Although the SM was built for FFF simulations, the concept can be applied for any thermally driven additive manufacturing process. Moreover, the approach introduced in this work can be generalized for various deposition patterns, process parameters (e.g. deposition speed), and different material properties. However, it would require much larger data sets to be generated for training. Nevertheless, the unique geometry parameterization (set of distances to the heat sources and sinks), time of deposition (from gcode), and definition of the HIZ is an important step to minimize the data required for the training of SM.

The SM paves the way towards achieving a real-time prediction and moves us closed to attain a closed loop control in the 3D printing paradigm. In the future, our goal is to build an SM for more complex geometries by introducing more detailed input parameters and using a more diverse range of process parameters.

Nomenclature

$(\bar{x}, \bar{y}, \bar{z})$	Location of instant heat source	m
α	Thermal diffusivity	m^2/s
$\bar{f}$	A surrogate model represented as a function	
$\bar{y}$	Output of a surrogate model	
$\boldsymbol{x}$	Array of input for a simulation	
δQ	Heat source	$W/m^2/K$
κ	Radiation coefficient	$W/m^2/K^4$
λ	Conductivity	$W/m/K$
Φ	CDF of a normal distribution	-
ρ	Density	kg/m^3
A_k	Area of influence of the k^{th} cooling surface	mm^2
C_d	Radius of deposition cross-section	mm
C_P	Specific heat	$J/kg/K$
d_b	Distance from the base	mm
d_c^k	Distance from the k^{th} cooling surface	mm
f	Simulation represented as a function	
h	Heat convection coefficient	$W/m^2/K$
h_d^i	Relative distance of nearby i^{th} deposition	mm
Q_d	Heat introduced due to deposition of unit length	J/m
q_{surf}	Flux through surface	W/m^2
$t, \bar{t}$	Time	s
T	Temperature	K
T_b	Base temperature	K

t_d^i	Relative time of nearby i^{th} deposition	s
T_∞	Temperature at infinite distance	K
T_{am}	Ambient temperature	K
T_t	Temperature at a point	K
V_d	Deposition speed	cm/s
y	Output of a numerical simulation	
ABS	Acrylonitrile Butadiene Styrene	
CF-PLA	Carbon Fiber polylactic acid	
FEM	Finite Element Model	
HIZ	Heat Influence Zone	-
SM	Surrogate Model	

References

[1] Sung-Hoon Ahn, Michael Montero, Dan Odell, Shad Roundy, and Paul K Wright. Anisotropic material properties of fused deposition modeling abs. *Rapid prototyping journal*, 8(4):248–257, 2002.

[2] M Atif Yardimci and Selçuk Güçeri. Conceptual framework for the thermal process modelling of fused deposition. *Rapid Prototyping Journal*, 2(2):26–31, 1996.

[3] Klaus-Jürgen Bathe. *Finite element procedures*. Klaus-Jurgen Bathe, 2006.

[4] Céline Bellehumeur, Longmei Li, Qian Sun, and Peihua Gu. Modeling of bond formation between polymer filaments in the fused deposition modeling process. *Journal of Manufacturing Processes*, 6(2):170–178, 2004.

[5] Anna Bellini and Selçuk Güçeri. Mechanical characterization of parts fabricated using fused deposition modeling. *Rapid Prototyping Journal*, 9(4):252–264, 2003.

[6] Sebastian Böck and Markus Schedl. Enhanced beat tracking with context-aware neural networks. In *Proc. Int. Conf. Digital Audio Effects*, pages 135–139, 2011.

[7] Bernhard E Boser, Isabelle M Guyon, and Vladimir N Vapnik. A training algorithm for optimal margin classifiers. In *Proceedings of the fifth annual workshop on Computational learning theory*, pages 144–152. ACM, 1992.

[8] Corinna Cortes and Vladimir Vapnik. Support-vector networks. *Machine learning*, 20(3):273–297, 1995.

[9] Alison Cozad, Nikolaos V Sahinidis, and David C Miller. Learning surrogate models for simulation-based optimization. *AIChE Journal*, 60(6):2211–2227, 2014.

[10] Bhaskar Dutta and FH Sam Froes. The additive manufacturing (am) of titanium alloys. *Metal powder report*, 72(2):96–106, 2017.

[11] Zak C Eckel, Chaoyin Zhou, John H Martin, Alan J Jacobsen, William B Carter, and Tobias A Schaedler. Additive manufacturing of polymer-derived ceramics. *Science*, 351(6268):58–62, 2016.

[12] Alexander Forrester, Andy Keane, et al. *Engineering design via surrogate modelling: a practical guide*. John Wiley & Sons, 2008.

[13] Jack Francis and Linkan Bian. Deep learning for distortion prediction in laser-based additive manufacturing using big data. *Manufacturing Letters*, 2019.

[14] M Frangos, Y Marzouk, K Willcox, and B van Bloemen Waanders. Surrogate and reduced-order modeling: a comparison of approaches for large-scale statistical inverse problems [chapter 7]. 2010.

[15] Tushar Goel and Nielen Stander. Comparing three error criteria for selecting radial basis function network topology. *Computer Methods in Applied Mechanics and Engineering*, 198(27):2137–2150, 2009.

[16] Mark Andrew Hall. Correlation-based feature selection for machine learning. 1999.

[17] Jan Hasenauer, Nick Jagiella, Sabrina Hross, and Fabian J Theis. Data-driven modelling of biological multi-scale processes. *Journal of Coupled Systems and Multiscale Dynamics*, 3(2):101–121, 2015.

[18] Thomas JR Hughes. *The finite element method: linear static and dynamic finite element analysis*. Courier Corporation, 2012.

[19] Emiliano Iuliano and Domenico Quagliarella. Proper orthogonal decomposition, surrogate modelling and evolutionary optimization in aerodynamic design. *Computers & Fluids*, 84:327–350, 2013.

[20] Ruichen Jin, Wei Chen, and Timothy W Simpson. Comparative studies of metamodelling techniques under multiple modelling criteria. *Structural and multidisciplinary optimization*, 23(1):1–13, 2001.

[21] Q Ye Kenny, William Li, and Agus Sudjianto. Algorithmic construction of optimal symmetric latin hypercube designs. *Journal of statistical planning and inference*, 90(1):145–159, 2000.

[22] Ron Kohavi and George H John. Wrappers for feature subset selection. *Artificial intelligence*, 97(1-2):273–324, 1997.

[23] Geoffrey M Laslett. Kriging and splines: an empirical comparison of their predictive performance in some applications. *Journal of the American Statistical Association*, 89(426):391–400, 1994.

[24] Stephen Leary, Atul Bhaskar, and Andy Keane. Optimal orthogonal-array-based latin hypercubes. *Journal of Applied Statistics*, 30(5):585–598, 2003.

[25] Longmei Li. *Analysis and fabrication of FDM prototypes with locally controlled properties*. University of Calgary, 2002.

[26] K Lindhorst, MC Haupt, and P Horst. Efficient surrogate modelling of nonlinear aerodynamics in aerostructural coupling schemes. *AIAA Journal*, 52(9):1952–1966, 2014.

[27] Jeffrey Lipton, Dave Arnold, Franz Nigl, Nastassia Lopez, DL Cohen, Nils Norén, and Hod Lipson. Multi-material food printing with complex internal structure suitable for conventional post-processing. In *Solid freeform fabrication symposium*, pages 809–815, 2010.

[28] Jeffrey I Lipton, Meredith Cutler, Franz Nigl, Dan Cohen, and Hod Lipson. Additive manufacturing for the food industry. *Trends in food science & technology*, 43(1):114–123, 2015.

[29] Michael D McKay, Richard J Beckman, and William J Conover. A comparison of three methods for selecting values of input variables in the analysis of output from a computer code. *Technometrics*, 42(1):55–61, 2000.

[30] Ferry PW Melchels, Marco AN Domingos, Travis J Klein, Jos Malda, Paulo J Bartolo, and Dietmar W Hutmacher. Additive manufacturing of tissues and organs. *Progress in Polymer Science*, 37(8):1079–1104, 2012.

[31] Douglas C Montgomery. *Design and analysis of experiments*. John Wiley & Sons, 2017.

[32] Mojtaba Mozaffar, Arindam Paul, Reda Al-Bahrani, Sarah Wolff, Alok Choudhary, Ankit Agrawal, Kornel Ehmann, and Jian Cao. Data-driven prediction of the high-dimensional thermal history in directed energy deposition processes via recurrent neural networks. *Manufacturing letters*, 18:35–39, 2018.

[33] Lawrence E Murr, Edwin Martinez, Krista N Amato, Sara M Gaytan, Jennifer Hernandez, Diana A Ramirez, Patrick W Shindo, Frank Medina, and Ryan B Wicker. Fabrication of metal and alloy components by additive manufacturing: examples of 3d materials science. *Journal of Materials Research and technology*, 1(1):42–54, 2012.

[34] Eric Neiva, Santiago Badia, Alberto F Martín, and Michele Chiumenti. A scalable parallel finite element framework for growing geometries. application to metal additive manufacturing. *arXiv preprint arXiv:1810.03506*, 2018.

[35] NT Nguyen, A Ohta, K Matsuoka, N Suzuki, and Y Maeda. Analytical solutions for transient temperature of semi-infinite body subjected to 3-d moving heat sources. *WELDING JOURNAL-NEW YORK-*, 78:265–s, 1999.

[36] Yew S Ong, Prasanth B Nair, and Andrew J Keane. Evolutionary optimization of computationally expensive problems via surrogate modeling. *AIAA journal*, 41(4):687–696, 2003.

[37] Art B Owen. Controlling correlations in latin hypercube samples. *Journal of the American Statistical Association*, 89(428):1517–1522, 1994.

[38] D Pal, N Patil, K Rafi, K Zeng, A Moreland, A Hicks, D Beeler, and B Stucker. A feed forward dynamic adaptive mesh refinement and de-refinement (ffd-amrd) strategy for problems with non-linear spatiotemporally periodic localized boundary conditions. *ASME J. Manuf. Sci. Eng*, 2014.

[39] Kurt Palmer and Kwok-Leung Tsui. A minimum bias latin hypercube design. *Iie Transactions*, 33(9):793–808, 2001.

[40] Samir Kumar Panda, Saumyakant Padhee, SOOD Anoop Kumar, and Siba Sankar Mahapatra. Optimization of fused deposition modelling (fdm) process parameters using bacterial foraging technique. *Intelligent information management*, 1(02):89, 2009.

[41] Nachiket Patil, Deepankar Pal, BE Stucker, et al. A new finite element solver using numerical eigen modes for fast simulation of additive manufacturing processes. In *Proceedings of the Solid Freeform Fabrication Symposium, Austin, TX, Aug*, pages 12–14, 2013.

[42] Nestor V Queipo, Raphael T Haftka, Wei Shyy, Tushar Goel, Rajkumar Vaidyanathan, and P Kevin Tucker. Surrogate-based analysis and optimization. *Progress in aerospace sciences*, 41(1):1–28, 2005.

[43] Junuthula Narasimha Reddy. *An introduction to the finite element method*, volume 2. McGraw-Hill New York, 1993.

[44] Junuthula Narasimha Reddy and David K Gartling. *The finite element method in heat transfer and fluid dynamics*. CRC press, 2010.

[45] José F Rodríguez, James P Thomas, and John E Renaud. Mechanical behavior of acrylonitrile butadiene styrene (abs) fused deposition materials. experimental investigation. *Rapid Prototyping Journal*, 7(3):148–158, 2001.

[46] M Roy and O Wodo. Quality assurance in additive manufacturing of thermoplastic parts: predicting consolidation degree based on thermal profile. *Int. J. of Rapid Manufacturing, Vol.*, (accepted):*, 2019.

[47] Moindze Soilahoudine, Christian Gogu, and Christian Bes. Accelerated adaptive surrogate-based optimization through reduced-order modeling. *AIAA Journal*, 2017.

[48] Michael Stein. Large sample properties of simulations using latin hypercube sampling. *Technometrics*, 29(2):143–151, 1987.

[49] John C Steuben, Andrew J Birnbaum, John G Michopoulos, and Athanasios P Iliopoulos. Enriched analytical solutions for additive manufacturing modeling and simulation. *Additive Manufacturing*, 25:437–447, 2019.

[50] Tom Stockman, Judith A Schneider, Bryant Walker, and John S Carpenter. A 3d finite difference thermal model tailored for additive manufacturing. *JOM*, pages 1–10, 2019.

[51] Gilbert Strang and George J Fix. *An analysis of the finite element method*, volume 212. Prentice-hall Englewood Cliffs, NJ, 1973.

[52] Q Sun, GM Rizvi, CT Bellehumeur, and P Gu. Experimental study of the cooling characteristics of polymer filaments in fdm and impact on the mesostructures and properties of prototypes. In *14th Solid Freeform Fabrication Symposium (SSF), Austin, TX, Aug*, pages 4–6, 2003.

[53] Q Sun, GM Rizvi, CT Bellehumeur, and P Gu. Effect of processing conditions on the bonding quality of fdm polymer filaments. *Rapid Prototyping Journal*, 14(2):72–80, 2008.

[54] Gustavo Tapia, Saad Khairallah, Manyalibo Matthews, Wayne E King, and Alaa Elwany. Gaussian process-based surrogate modeling framework for process planning in laser powder-bed fusion additive manufacturing of 316l stainless steel. *The International Journal of Advanced Manufacturing Technology*, pages 1–13, 2017.

[55] Nahum Travitzky, Alexander Bonet, Benjamin Dermeik, Tobias Fey, Ina Filbert-Demut, Lorenz Schlier, Tobias Schlordt, and Peter Greil. Additive manufacturing of ceramic-based materials. *Advanced Engineering Materials*, 16(6):729–754, 2014.

[56] Jun Wang, Sonjoy Das, Chi Zhou, and Rahul Rai. Data-driven simulation for fast prediction of pull-up process in bottom-up stereo-lithography. In *ASME 2016 International Design Engineering Technical Conferences and Computers and Information in Engineering Conference*, pages V01AT02A035–V01AT02A035. American Society of Mechanical Engineers, 2016.

[57] Kenny Q Ye. Orthogonal column latin hypercubes and their application in computer experiments. *Journal of the American Statistical Association*, 93(444):1430–1439, 1998.

[58] Y Zhang and K Chou. A parametric study of part distortions in fused deposition modelling using three-dimensional finite element analysis. *Proceedings of the Institution of Mechanical Engineers, Part B: Journal of Engineering Manufacture*, 222(8):959–968, 2008.

[59] Y Zhang and YK Chou. Three-dimensional finite element analysis simulations of the fused deposition modelling process. *Proceedings of the Institution of Mechanical Engineers, Part B: Journal of Engineering Manufacture*, 220(10):1663–1671, 2006.

[60] Andrea Zocca, Paolo Colombo, Cynthia M Gomes, and Jens Günster. Additive manufacturing of ceramics: issues, potentialities, and opportunities. *Journal of the American Ceramic Society*, 98(7):1983–2001, 2015.

Appendix

Process modeling for FFF

In this section, we briefly describe the mathematical formulations that govern the thermal behavior in an extrusion-based AM process. The critical phenomenon that controls the thermal behavior in an AM process includes: conduction within the deposited layers and subsequent cooling, convection and radiation from the free surfaces, the evolution of the free surfaces as the deposition proceeds, continuous material deposition and associated heat introduction with the additive domain. Moreover, additional process and system variables affect the thermal behavior of the process, such as the ambient temperature, layer size, deposition patterns, deposition speed, and deposition temperature.

Modeling of the FFF process has seen limited progress regarding its thermal behavior compared to the metal printing processes. Yardimci and Güçeri [2], and Li [25] were pioneer researchers to model the transient heat transfer in FFF. Rodriguez [45] considered the elliptical shape of the filament and proposed a numerical model that accounts for its effects. In this article, we concentrate on the thermal behavior of the process and model it using finite element method (FEM).

The thermal behavior within the deposited material can be mathematically formulated as a transient heat equation:

$$\frac{\partial \left(\rho C_p T\right)}{\partial t} = \nabla \left(\lambda \nabla T\right) \tag{9}$$

where, T is the temperature, ρ is the density of the deposited material, λ is the thermal conductivity. The boundary conditions account for the interaction of the printed material with the environment. The top and side free surfaces of the printed part is exposed to the ambient condition. The bottom of the part is in direct contact of the heated base of the printer. The cooling effect at the surface is due to convection and radiation. It is modeled as a following boundary condition (BC), and it is applied on free outer surfaces of the printed part:

$$Q_{surf} = h(T - T_{am}) + \kappa(T^4 - T_{\infty}^4) \tag{10}$$

where, h is the heat convection coefficient of the material at the ambient temperature, T_{am} is the printing chamber temperature during the print, T_{∞} is the reference temperature at an infinite distance for radiation. In the process of FFF, the ambient temperature is assumed to be minutely affected by the deposition and hence, $T_{\infty} = T_{am}$. Another set of boundary conditions correspond to the heating through the base is modeled as a Dirichlet boundary condition. The base is assumed to be at a constant temperature of T_b. The deposition temperature (T_d) is modeled as the initial condition for the deposited material.

There are two main complexities involved in solving the mathematical model:

1. Evolving boundary and surface tracking: The printing process continuously increases the size of the domain and changes the location of free surfaces. To apply the BCs, tracking the surface at every instance of time is essential.

Table 2: Simulation details

Material properties	Conduction coefficient (λ)	0.17 $W/m/K$
	Emissivity for air (κ)	0.90
	Convection coefficient (h)	21 $W/m^2/K$
	Density (ρ)	1050 kg/m^3
	Specific heat (C_P)	2020 $J/kg/K$
Process parameters	Layer thickness	0.0002 m
	Road width	0.0004 m
	Ambient temperature (T_{am})	303.15 K
	Base temperature (T_b)	358.15 K
	Print speed (ν)	0.03 m/s
Mesh details	Element size	$0.0001 \times 0.0001 \times 0.0001$ m
	Element type	8 node linear thermal brick element(DC3D8)
	Integration	Full integration
Deposition details	Activation length	0.0004 m
	Initial Condition (T_d)	503.15 K (Temperature)
	Activation set size	$0.0004 \times 0.0001 \times 0.0002$ m

2. Moving heat source and deposition: The material is deposited at a high temperature and, due to continuous deposition, it behaves as a continuously moving heat source. Therefore, the heat source needs to be traced at every time interval.

The governing equations eqs. (9) and (10) are evaluated in ABAQUS® – a commercial software based on the finite element method [18, 3, 43, 44, 51]. Although ABAQUS® is used to solve the governing equations in FEM, the mesh of the model is created using an in-house code. The continuous deposition of the physical process is modeled as discrete depositions in small time intervals. The mesh is numbered to facilitate the gradual activation of these depositions that follows the printing path. The discrete depositions are implemented as groups of elements (also known as sets) that constitute the deposition units. As the printing proceeds, new elements sets are added to the mesh with 'precondition' temperature matching deposition temperature, T_d. Moreover, the boundary conditions are applied on the outer free surfaces of the deposition set. For the entire part, the bottom surface is subjected to constant temperature T_b. The side and top surfaces of the entire print have applied external convection and radiation fluxes given by equation 10.

The deposited roads have a small cross-section (0.16 mm^2) that is discretized into eight elements with the size of the element 0.001 mm^3. With such discretization, the mesh for a print of a 1000 mm^3 results in approximately 1 million degrees of freedom. The details of the material properties and discretization is given in Table 2. As in any modeling, certain assumptions are made while ensuring that key phenomena in the layer-by-layer deposition are accounted for. Nevertheless, several assumptions are taken into account to generate data for training. First of all, the material is assumed to be

homogeneous and isotropic. Deposited roads are rectangular in cross-section and are in perfect contact. The properties of the material are assumed to be constants. Similarly, the ambient temperature (T_{am}) and base temperature (T_b) are considered constant during the process.

Heat Influence Zone (HIZ)

The HIZ determines the size of the neighborhood significantly affected by the heat source. The size of HIZ can be analytically calculated using the transient solution of a point source on a semi-infinite body [35]. The temperature change due to a heat source can be represented as,

$$\frac{dT}{dt} = \frac{\delta\dot{Q}}{\rho C_p \left[4\pi\alpha\left(t-\bar{t}\right)\right]^{3/2}} \exp\left(-\frac{(x-\bar{x})^2+(y-\bar{y})^2+(z-\bar{z})^2}{4\alpha\left(t-\bar{t}\right)}\right) \tag{11}$$

where, T is the temperature at point (x, y, z) at time t. Coefficient α is the thermal diffusivity defined as $\alpha = \lambda/\rho C_P$. The location of the instantaneous heat source ($\delta\dot{Q}$) at time t is $(\bar{x}, \bar{y}, \bar{z})$. The heat source was introduced in the system at time $\bar{t}$.

Since the influx ($\delta\dot{Q}$) in Equation 11 is linearly related to the increment in temperature (dT/dt), multiple instances of point heat source can be superposed to get their cumulative effect. The heated depositions are quantified in terms of introduced heat to get their HIZ. Let us consider a small deposition of size (a, b, c) on a printed part. The deposition can be considered as a volumetric heat source with initial temperature (T_d). Each point in this small deposition can be considered as a point heat source.

Considering the coordinate system as given in the figure, we get,

$$\frac{dT}{dt} = \int_{a_1}^{a_2}\int_{b_1}^{b_2}\int_{c_1}^{c_2} \frac{\delta\dot{Q}}{\rho C_p \left[4\pi\alpha\left(t-\bar{t}\right)\right]^{3/2}} \exp\left(-\frac{(x-\bar{x})^2+(y-\bar{y})^2+(z-\bar{z})^2}{4\alpha\left(t-\bar{t}\right)}\right) d\bar{z}d\bar{y}d\bar{x} \tag{12}$$

where, (a_1, b_1, c_1) and (a_2, b_2, c_2) are the coordinates of the two diagonally opposite vertices of the unit deposition. Simplifying Equation 12 we can get

$$\frac{dT}{dt} = \gamma \int_{a_1}^{a_2} \exp\left(-\frac{(x-\bar{x})^2}{4\alpha\left(t-\bar{t}\right)}\right) d\bar{x} \cdot \int_{b_1}^{b_2} \exp\left(-\frac{(y-\bar{y})^2}{4\alpha\left(t-\bar{t}\right)}\right) d\bar{y} \cdot \int_{c_1}^{c_2} \exp\left(-\frac{(z-\bar{z})^2}{4\alpha\left(t-\bar{t}\right)}\right) d\bar{z} \tag{13a}$$

$$\gamma = \frac{\delta\dot{Q}}{\rho C_p \left[4\pi\alpha\left(t-\bar{t}\right)\right]^{3/2}} \tag{13b}$$

Let us consider a cumulative distribution function (CDF) of a normal distribution,

$$\Phi(a|\mu,\sigma) = \frac{1}{\sigma\sqrt{2\pi}} \int_{-\infty}^{a} e^{-\frac{(g-\mu)^2}{2\sigma^2}} dg \tag{14}$$

where, g is the random variable, a is a value of random variable at which CDF is being calculated, μ is the mean and σ is the standard deviation. Lets define g, μ and σ for the present context as:

$$g = \bar{x}, \bar{y} \ or \ \bar{z} \tag{15a}$$

$$\mu = x, y \ or \ z \tag{15b}$$

$$\sigma = \sqrt{2\alpha(t - \bar{t})} \tag{15c}$$

Substituting these definitions in Equation 14 and replacing them in the Equation 13a, we get the following simplified equation:

$$\frac{dT}{dt} = \frac{\delta\dot{Q}}{\rho C_p} \left((\Phi(a_2|x,t) - \Phi(a_1|x,t)) \left(\Phi(b_2|y,t) - \Phi(b_1|y,t)\right) \left(\Phi(c_2|z,t) - \Phi(c_1|z,t)\right)\right) \tag{16}$$

This equation yields the temperature T at any point due to the uniform heat source.

$$T(x,y,z,\tau) = \int_0^\tau \frac{\delta\dot{Q}}{\rho C_p} \left((\Phi(a_2|x,t) - \Phi(a_1|x,t)) \left(\Phi(b_2|y,t) - \Phi(b_1|y,t)\right) \left(\Phi(c_2|z,t) - \Phi(c_1|z,t)\right)\right) dt \tag{17}$$

where Φ is cumulative distribution function of a normal distribution and $T_\tau(x,y,z)$ is the temperature at the point with coordinate(x,y,z) at time τ. The heat source is assumed to be static in Equation 17. In this case the heat introduced into the system per unit volume is:

$$\delta Q = \rho C_P \left(T_d - T_{end}\right) \tag{18}$$

where, T_{end} is the final temperature of the system. The deposition is a moving heat source.

Equation 17 is implemented to determine the HIZ in ABS and CF-PLA plastic in Section 3.2. The HIZ provides a conservative estimate of the neighborhood of interest around any point of the printed part. To get the estimated HIZ, we deposit 20 roads of length 4 mm and height 0.2 mm on a cuboid part of 10 mm in height and $4 \times 4\,\text{mm}^2$ in cross-section. The integration is evaluated in small time steps of 0.01 s till the maximum temperature of the part decreases below 10% of the glass temperature. The flux from the heated deposition is updated every time step as $\dot{q} = h(T_d^t - T_b^t)$, where T_d^t is the temperature of the deposited part at time t and T_b^t is the temperature of the contact surface at the same time. Thus value of the parameters in Equation 17 becomes as follows:

Parameters	Values (m)
(a_1, a_2)	$(-0.002, 0.002)$
(b_1, b_2)	$(-0.002, 0.002)$
(c_1, c_2)	$(-0.0001, 0.0001)$